AFOSR-TR- 79 - 13 2 1

█A079646

RTI/1437/00-02F
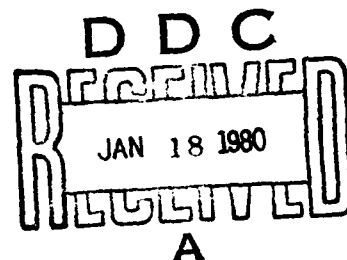
QUATERNARY ALLOY MICROWAVE MESFET

Final Report on
AFOSR Contract No. F49620-77-C-0062

J. W. Harrison, Principal Investigator
S. B. Phatak
G. Kelner
M. A. Littlejohn
A. F. Schreiner
H. H. Stadelmaier
J. Hsu
R. J. Trew

D D C
RECEIVED
JAN 18 1980
RECEIVED
A

Research Triangle Institute
Research Triangle Park, North Carolina    27709

Approved for public release; distribution unlimited

Air Force Office of Scientific Research
Directorate of Electronic and Solid State Sciences
Bolling AFB, District of Columbia    20332

80    1  16  021

| REPORT DOCUMENTATION PAGE | | READ INSTRUCTIONS BEFORE COMPLETING FORM |
|---|---|---|
| 1. REPORT NUMBER  AFOSR TR-79-1321 | 2. GOVT ACCESSION NO. | 3. RECIPIENT'S CATALOG NUMBER |
| 4. TITLE (and Subtitle)  Quaternary Alloy Microwave MESFET | | 5. TYPE OF REPORT & PERIOD COVERED  Final Technical Report 3/1/77 - 9/30/79 |
| | | 6. PERFORMING ORG. REPORT NUMBER  RTI/1437/00-02F |
| 7. AUTHOR(s)  J. W. Harrison, G. Kelner  S. B. Phatak, H. H. Stadelmaier  M. A. Littlejohn | | 8. CONTRACT OR GRANT NUMBER(s)  F49620-77-C-0062 |
| 9. PERFORMING ORGANIZATION NAME AND ADDRESS  Research Triangle Institute  P.O. Box 12194  Research Triangle Park, NC 27709 | | 10. PROGRAM ELEMENT, PROJECT, TASK AREA & WORK UNIT NUMBERS  2306/B2  61102F |
| 11. CONTROLLING OFFICE NAME AND ADDRESS  Air Force Office of Scientific Research  Building 410  Bolling AFB, DC 20332 | | 12. REPORT DATE  30 November 79 |
| | | 13. NUMBER OF PAGES  86 |
| 14. MONITORING AGENCY NAME & ADDRESS(if different from Controlling Office)  2306 | | 15. SECURITY CLASS. (of this report)  Unclassified |
| | | 15a. DECLASSIFICATION/DOWNGRADING SCHEDULE |

16. DISTRIBUTION STATEMENT (of this Report)

Approved for public release; distribution unlimited.

17. DISTRIBUTION STATEMENT (of the abstract entered in Block 20, if different from Report)

Final technical rept.
1 mar 77-30 Sep 79

18. SUPPLEMENTARY NOTES

19. KEY WORDS (Continue on reverse side if necessary and identify by block number)

MESFET  Liquid Phase Epitaxy
GaInAsP
InP
Quaternary Alloy

20. ABSTRACT (Continue on reverse side if necessary and identify by block number)

Liquid phase epitaxial growth techniques have been used to grow quaternary alloys, $Ga_{1-x}In_xP_{1-y}As_y$ on InP substrates, using (100), (111) A and (111) B orientations. Liquidus and solidus data at 660°C have been used to determine distribution coefficients for P, As, and Ga in the melt. Compositions lattice matched to InP have been grown as single crystals. A preliminary X-ray evaluation of structure
(over)

(Block 20)                                                    $S_Q$ $\epsilon_M$

shows no detectable long-range ordering. Best electronic properties
to date have been a Hall mobility of 4000 $cm^2$/V-sec at room temperature
with a carrier concentration of 3.8 $\times 10^{16}$ $cm^{-3}$ in material which has
not been intentionally doped. Deposition of gold contacts on alloy
samples yielded nonlinear current-voltage characteristics, but with
poorly defined barriers.

TIMES TEN TO THE 16 TH POWER
PER CC

## TABLE OF CONTENTS

A. D. L.....
Technical In... ... Officer

# LIST OF FIGURES

## LIST OF TABLES

# 1.0 INTRODUCTION AND SUMMARY

Theoretical work performed under Air Force contract [1] has indicated that some $Ga_{1-x}In_xP_{1-y}As_y$ alloy compositions that are lattice matched to InP have electronic properties which give them the potential for use in high frequency MESFET devices which will perform significantly better than those made with GaAs. As an example, the projected gain-bandwidth product for a MESFET made with $Ga_{0.27}In_{0.73}P_{0.4}As_{0.6}$ is about 2.3 times that for one made with GaAs using the same device dimensions and doping level.

Although the growth by liquid phase epitaxy (LPE) of $Ga_{1-x}In_xP_{1-y}As_y$ lattice matched to InP [2-4] and to $GaP_{1-y}As_y$ [5] substrates had been reported prior to mid 1976, the compositions and doping levels used were appropriate to optoelectronic devices rather than to MESFET fabrication. The latter operation requires very thin (on the order of 0.2 to 0.4 µm) epitaxial layers of high crystalline perfection. This implies an excellent lattice match to the substrate, which must be semi-insulating in order to avoid spurious conduction and, furthermore, must itself be of high crystalline perfection in order to minimize the formation of electrically active defects at the substrate-epilayer interface.

In August 1976 the Research Triangle Institute (RTI) proposed to the Air Force Office of Scientific Research a research effort to synthesize a quaternary alloy material and use this material in a prototype MESFET to enable comparison of performance with similar devices made from GaAs.

This research program was envisioned as a three-year effort with the following major objectives:

1. To demonstrate LPE growth of the desired $Ga_{1-x}In_xP_{1-y}As_y$ alloy composition.

2. To use compositional and structural analysis to guide the growth process in order to obtain epitaxial material of the highest possible perfection.

3. To perform electronic properties measurements to verify theoretical predictions of enhanced properties relative to GaAs.

4. To identify and demonstrate suitable ohmic and Schottky barrier metallization materials necessary for MESFET fabrication.

5. To fabricate and demonstrate prototype MESFET design using the the best material produced and to relate the performance of this device to material properties.

Prior theoretical calculations [6] had indicated that the presence of compositional disorder in the lattice arrangement of the $Ga_{1-x}In_xP_{1-y}As_y$ alloys could introduce a scattering mechanism (so-called "alloy scattering") which could reduce electron mobility and, therefore, performance of devices made from disordered alloys. One of the correlations sought in the proposed research was that between compositional disorder and electronic properties.

This proposal was accepted by AFOSR, and the first year funding started March 1, 1977. The first year efforts have been previously reported [7]. Growth efforts during the first year were directed first to compositional control to obtain alloys lattice matched to InP substrates, particularly those compositions near $Ga_{0.72}In_{0.73}P_{0.4}As_{0.6}$. Theoretical calculations [6] of velocity-field characteristics had indicated that a range of alloy compositions lattice matched to InP provided transport properties that made them potentially superior to GaAs in MESFET fabrication. The capability for

2

growth of good quality epitaxial layers on (111)B oriented InP substrates was demonstrated.

Although the quaternary layers were of good crystallographic quality, the electrical properties were not as desired. Even in non-intentionally doped material, electron carrier concentrations were large, initially on the order of $10^{18}$ cm$^{-3}$. Improved melt bake-out procedures and the use of higher purity source materials enabled the reduction of carrier concentrations to the range $4 \times 10^{16}$ to $2 \times 10^{17}$ cm$^{-3}$. The highest electron mobility value obtained was about 4,000 cm$^2$/V-sec at a carrier concentration of $3.8 \times 10^{16}$ cm$^{-3}$, with both measurements made at room temperature. This value for mobility was about half the predicted (theoretical) value. The use of InP buffer layers between the InP substrate and the quaternary layer appeared to have no effect on layer properties.

Photoluminescence measurements for the quaternary alloy layers made early in the program showed the presence of deep levels, but well before the end of the first year's efforts, these deep levels had been eliminated; and the emissions from the quaternary alloys were intense band-to-band transition lines of narrow width, indicating, along with the improvement in electrical properties, that the growth process was yielding much better quality layers.

As a means of measuring structural order (for correlation to electronic properties), X-ray diffraction measurements were attempted. This required removal of the InP substrate to allow direct exposure of the epitaxial quaternary layer to the X-ray beam. The fragility of the thin (5 to 10 μm) exposed epilayers created many problems in sample preparation. This necessitated the development of a selective etch that dissolved the InP substrate material at a much higher rate than the quaternary alloy

material. With this etch suitable samples for X-ray analysis were being prepared near the end of the first year's effort.

Attempts to make Schottky barriers on the quaternary material were not successful during the first year. Although I-V characteristics for the structures formed by deposition of gold on the quaternary were nonlinear, there did not appear to be any well-defined barrier.

During the second year quaternary growth was carried out on (111)A and (100) oriented InP substrates as well as (111)B for a total of 140 growth runs. Many of these runs were required to work out the phase diagram, particularly for the (111)A face, to enable compositional control over the quaternary epilayer. Lattice mismatch between the epilayer and InP substrate was, for many layers, reduced to below the limit of detection (±0.03 percent in our case). Thickness control of about ±20 percent was achieved for epilayers of 1 to 5 μm thickness. For submicron layers, however, growth rate variations from run to run were much larger. Further work is needed to achieve precise control. Distribution coefficients for the n-type dopant species—tin, tellurium, and selenium—were determined.

Photoluminescence and X-ray diffraction measurements indicated high crystalline quality and homogeneity for those layers grown after phase diagram data enabled precise composition control to achieve lattice match between the alloy epilayers and InP substrates. The use of (111)A and (100) oriented epilayer layers enabled relatively straightforward preparation of samples for X-ray analysis to ascertain order. Low intensity diffraction peaks, which could possibly be interpreted as due to the presence of a tendency to long-range order, were detected; but the degree of ordering was not quantified. In general, experimental difficulties prevented the collection of enough X-ray diffraction data to enable

4

correlation of the degree of lattice ordering with growth conditions and electronic properties.

Conductivity and Hall effect measurements indicated that even though the non-intentional carrier concentrations were reduced to about $10^{16}$ cm$^{-3}$, there was no improvement in carrier mobility over t· it obtained during the first year. Room temperature values of mobility in doped and undoped layers were typically 2,000 to 3,000 cm$^2$/V-sec. This was far below theoretically predicted values. An analysis of mobility versus temperature data indicates that the epilayers probably contain a large number of inhomogeneities that give large components of space charge scattering and, possibly, dislocation scattering.

No problems were experienced in making ohmic contacts to the quaternary alloys, but efforts to obtain stable and reproducible Schottky barriers were for the most part not successful. Five different metals were investigated: Au, Al, Cr, Ag, and Mg. Of these, only Au provided appreciably nonlinear I-V characteristics. The largest barrier height obtained was 0.51 volt and a diode factor n = 2.6.

A preliminary design for X and $K_a$ band MESFETs was undertaken, but because of the low mobility values and difficulty in obtaining good Schottky barriers, actual fabrication of devices was not carried out.

There still appear to be many problems to be worked out before microwave MESFET device quality $Ga_{1-x}In_xP_{1-y}As_y$ material can be routinely achieved.

## 2.0 MATERIAL GROWTH

### 2.1 Liquid Phase Epitaxy

For LPE growth, standard horizontal slider boats made of high purity graphite were used. Two different LPE reactors were committed to this program this year. One was the Lindberg "Heavy-Duty" furnace described in the previous annual report [7]. The second furnace was constructed at RTI. It consists of "clam-shell" type resistance heaters containing a 60-cm long liquid sodium-filled heat pipe mounted on wheels which run on a track arrangement that allows the entire furnace to be pulled over the quartz reactor tube. Fast heat up and cool down can be realized this way. In addition, the heat pipe allows a flat temperature zone approximately 25 cm long.

The LPE growth procedure used in most experiments was the same as that described in the previous annual report [7]--i.e., the "transient method" with ramp cooling was utilized for most of the growth runs. However, for certain specific experiments, to be described later, the "step cooling" approach was used. In these cases the melt was saturated at a given temperature, $T_s$, (in the range 650-640°C) and was then subjected to a rapid cooling step of $\Delta T_s$ varying between 2 and 10°C to cause supersaturation in the melt. In our furnaces such a drop in temperature can be achieved in two to six minutes. Once the temperature had stabilized, substrate wafers were inserted in the melt for the desired length of time for LPE growth to occur, typically ten minutes.

Finally, for a few growth runs with (100) oriented substrates, the "two-phase" method [2-4] was utilized in conjunction with step cooling. In this case the melt was an undersaturated solution of Ga, In, and As

into which an excess of solid InP was introduced in order to supply the required amount of phosphorous to the melt. With this method, growth occurs on the InP substrate as well as on the solid phase InP present in the melt.

In order to facilitate analyses by X-ray techniques to determine the state of ordering in these quaternary compounds, it was found desirable that epilayers should be grown on either the (111)A or (100) faces of InP substrate crystals. This was concluded primarily because of the ease in preparing samples suitable for X-ray analysis. In this year's effort, more than 140 growth runs have been made employing more than 150 substrates. Of these, over 45 runs were made on (111)A, 14 on (100), and the remainder on (111)B oriented substrates. All the effort was directed primarily toward the composition $Ga_{0.27}In_{0.73}As_{0.60}P_{0.40}$ although other compositions have also been grown. On (111)B substrates this composition was realized last year and can now be grown reproducibly and routinely. On the (111)A face, however, the phase diagram is unknown in this composition range. Hence the epilayer compositions obtained encompassed a relatively wide range due to the exploratory nature of the investigation.

## 2.2  Phase Diagram Data

During liquid phase epitaxy, growth parameters such as distribution coefficients, $k_i$, for different atomic species ($k_i = C_i^s/C_i^\ell$, where $C_i^s$ and $C_i^\ell$ are concentrations in the solid and liquid phases, respectively; i = Ga, In, As, or P) and layer morphology are dependent upon substrate orientation. Therefore, to obtain the same epitaxial layer composition on different substrates, the melt composition has to be varied. Thus liquidus isotherms of the phase diagrams have to be determined for new melt

8

composition ranges. The experimental procedure used for this is the source dissolution method described in Reference 7. Briefly, a melt with known Ga atom fraction, $x_{Ga}^{\ell}$ (or the In/Ga ratio), is prepared, and a known amount of As (in the form of InAs) is added. Then this melt is saturated with an InP source wafer to establish thermodynamic equilibrium between InP and the melt. It has been found that a period of two hours at 650°C is adequate for this process for small (3 to 4 g) melts. From weight loss measurements on the InP source wafer, equilibrium melt composition can then be determined. Numerous such experiments were conducted, and the results are shown in Figure 1. Here it is seen that for any given gallium concentration, $x_p^{\ell}$ decreases with increasing $x_{As}^{\ell}$, as is to be expected. Also it is to be noted that only a small amount of phosphorous is present in the melt, reflecting its high distribution coefficient ($k_p$). Further, the small amount of InP dissolved in the melt presents problems in weight loss measurement. In Figure 2, $k_i$ is plotted as a function of y for $Ga_{1-x}In_xP_{1-y}As_y$ epitaxial layers grown on (111)A face. Data for growth on (100) and (111)B orientations are also included in this figure. The data for (100) face were obtained from published work [4,5] and our own work.

## 2.3  Doping

Three donor-type impurities--Sn, Te, and Se--were used to obtain carrier densities of about $10^{17}$ $cm^{-3}$ or above in the $Ga_{1-x}In_xP_{1-y}As_y$ alloys. All three were found to be well behaved, shallow-level donors with a doping behavior similar to that experienced with InP but with slightly different distribution coefficients. Our data are presented in Table 1 for alloy layers grown on (111)B oriented substrates at 650°C. Also shown are data for InP [8,9] for purposes of comparison.
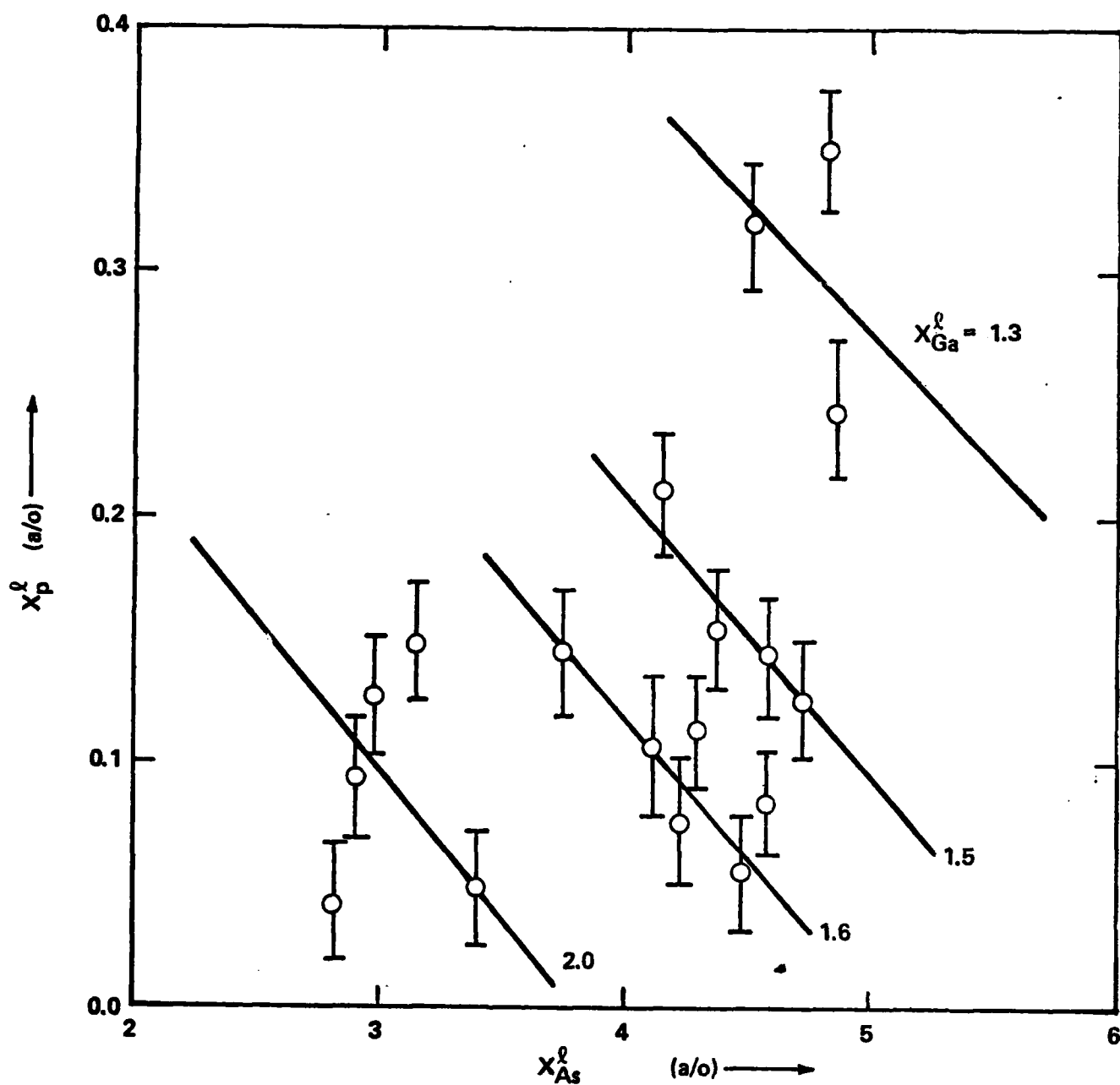
Figure 1. Liquidus curves at 650°C showing dependence of phosphorous solubility on concentration of arsenic in GaInAsP melts. Running parameter is gallium atom fraction.
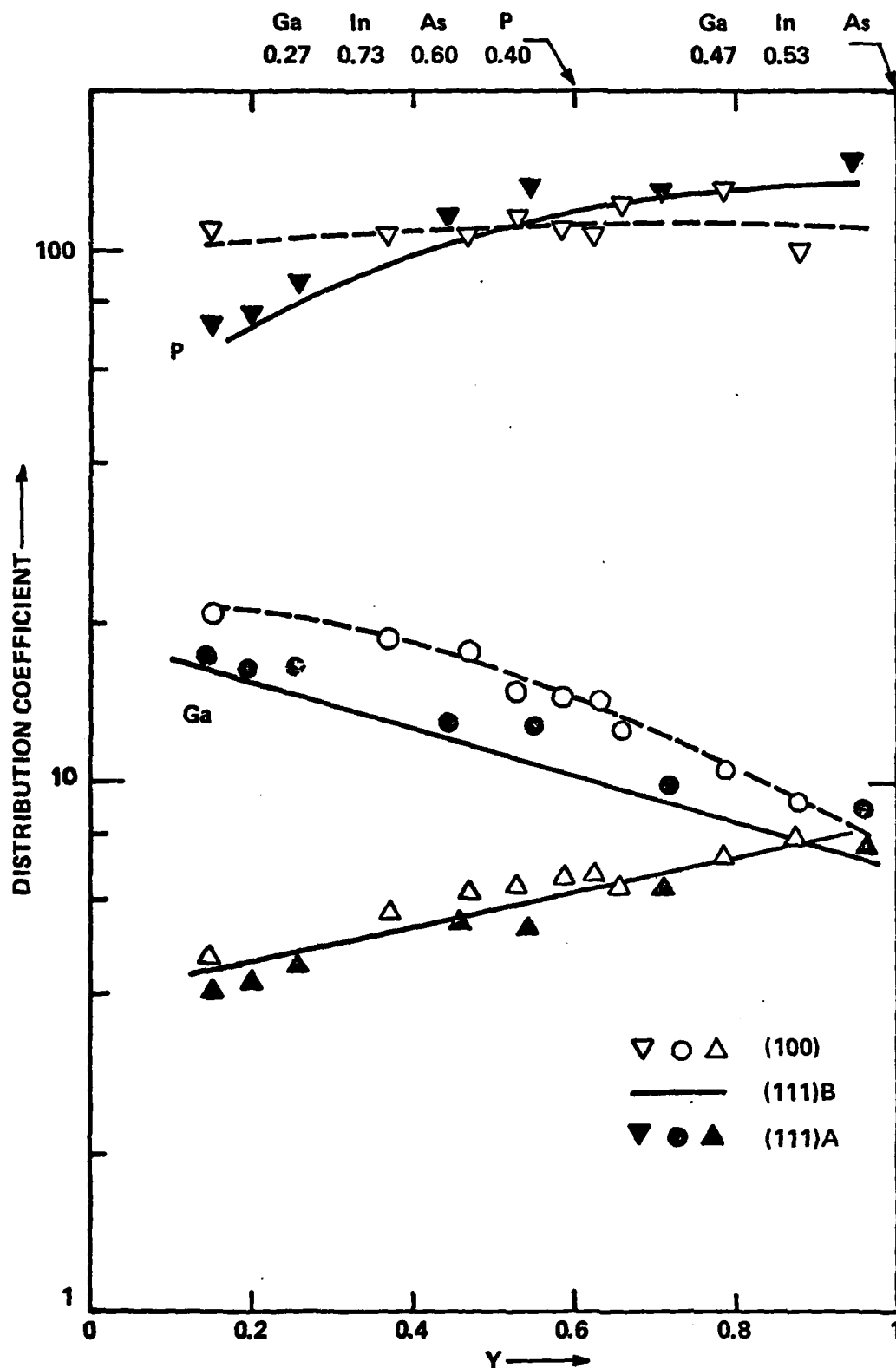
Figure 2. Distribution coefficients of Ga, As and P on (100), (111) A and (111) B InP substrates in the epitaxial layer composition range 0<y<1.

Table 1. Distribution Coefficients of Donor Atoms at 650°C

| Donor | InP | $Ga_{0.27}In_{0.73}As_{0.60}P_{0.40}$ |
|:---:|:---:|:---:|
| Ge | 0.011 | |
| Sn | 0.0022 | 0.002 |
| Te | 0.4 | 0.35 |
| Se | 4.2 | ~1.0 |
| Si | 40.0 | |

## 2.4 Morphology

Although it is easy to chemically process (100) oriented substrates for preparing X-ray analysis samples, it has other limitations. The main problem is in the growth of thick (25 to 30 μm) layers. When layers of such high thickness are precipitated from a melt, the layer composition changes over its thickness, resulting in a changing lattice parameter. This leads to a severely strained, and in extreme cases polycrystalline, layer, since (100) orientation in zinc-blende structures cannot accommodate significant lattice mismatch. This problem deserves special attention in any future work.

Generally, the crystalline quality and morphology of thinner (1 to 5 μm) layers has been excellent and has been improved substantially over that from last year. This is evidenced by the sharp line widths obtained from both X-ray diffraction and photoluminescence peak widths. In particular, lattice mismatch between epilayer and substrate has been reduced to below the limit of detection, which in our case is about ±0.03 percent.

The control of layer thickness has been improved and is better than ±20 percent for layers 1 to 5 μm thick. For thinner, submicron layers,

the growth rate variation was much larger. Further work is needed to achieve precise control.

# 3.0 MATERIAL PROPERTIES

## 3.1 <u>Composition and Structure</u>

Composition of the quaternary epitaxial layers was determined by electron probe microanalysis (EPMA). In addition, single-crystal X-ray diffraction (XRD) and photoluminescence (PL) measurements were used to measure the lattice parameter $(a_o)$ and energy bandgap $(E_g)$, respectively. As in the past, $a_o$ and $E_g$ have also been used to compute the composition of epitaxial layers by using published parametric equations [10, 11, 12]. These measurements are also used as a measure of the quality of epitaxial layers: Narrow XRD and PL peaks indicate high crystalline quality and homogeneity. Figure 3 illustrates some XRD profiles for samples with zero and nonzero lattice mismatch. In this figure the intensity of the diffracted X-ray beam is plotted (in arbitrary units) against the diffraction angle, 2 $\theta$. A Cu target tube was used for this measurement, which yielded a doublet pair, $K\alpha_1$-$K\alpha_2$, with wavelengths of 1.5405 and 1.5443 Å, respectively. Bare InP substrate crystals of good crystalline quality can resolve this doublet extremely well with a 2 $\theta$ separation of 0.6 degree and a FWHM of approximately 9'. With GaInAsP quaternary layers on InP substrates, two sets of diffraction peaks $(K\alpha_1, K\alpha_2)$ are distinguishable, arising from the epitaxial layer and the substrate. If the epitaxial layer is lattice matched, the peaks merge together and only one pair of peaks is visible. In Figure 3, Sample Q-2-016 shows this situation. Here the $K\alpha_1$ peak has a FWHM of approximately 12', slightly greater than the 9' obtained for the underlying InP substrate. Diffraction profiles for Samples Q-2-015 and Q-2-027 show small shoulders to the left and right, respectively. For Q-2-016, since the peaks are merged completely, it can
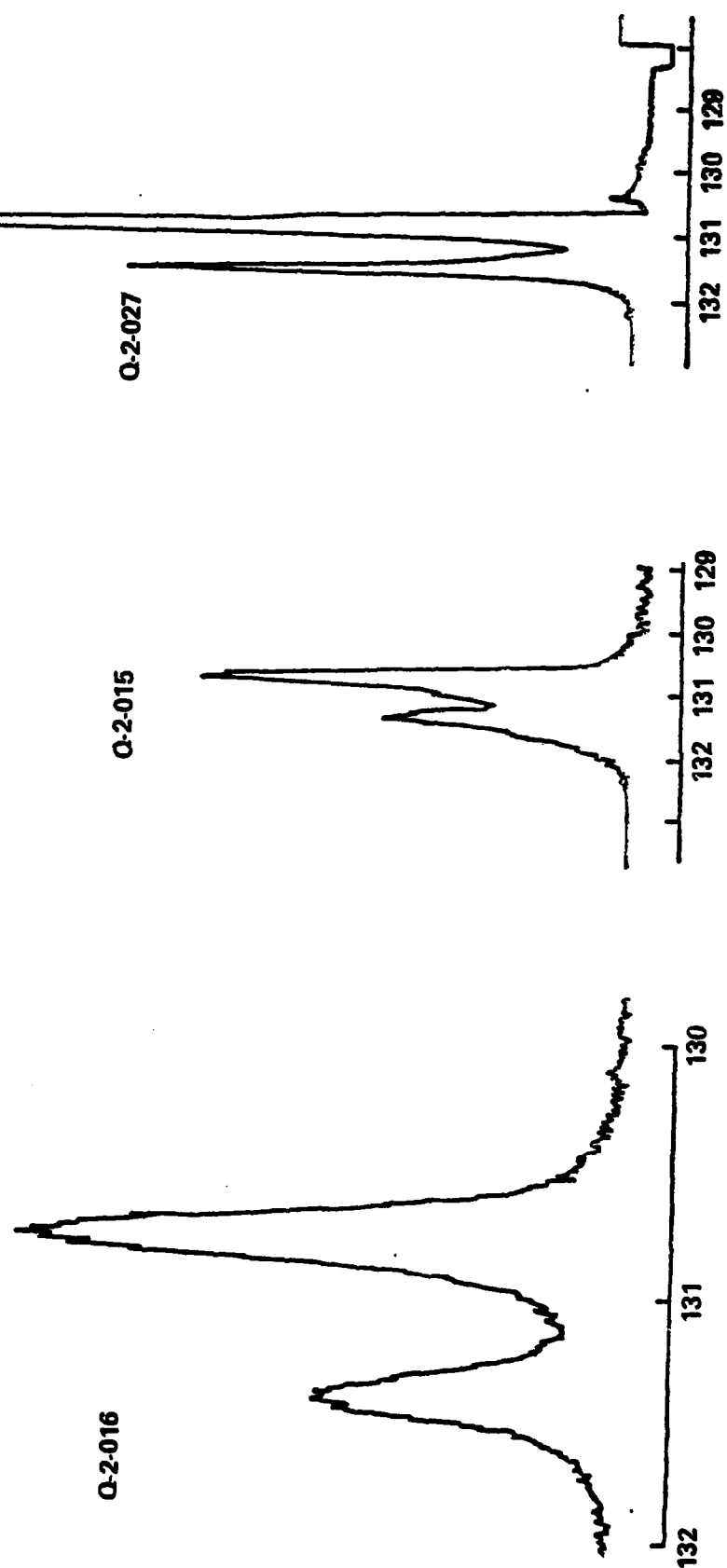
Figure 3. X-ray diffraction profiles for GaInAsP layers. Diffracted X-ray intensity (arbitrary units) is plotted vs. diffraction angle $2\theta$ for three samples, showing from left, $\Delta s \pm 0.03\%$, $\Delta a = -0.04\%$, $\Delta a = 0.04\%$.

only be deduced that the mismatch is less than ±0.03 percent, the detection limit. Exactly what is represented by this peak broadening is not clear yet, although minor gradients in lattice parameter or a defect-strained lattice could certainly be responsible.

Table 2 lists PL peak widths for some samples. It is seen that these peaks have a FWHM ranging from about 50 to 80 meV at room temperature, which compares favorably with published data [13].

As reported previously [7], X-ray diffraction measurements had revealed the presence of weak, but detectable, lines which signaled the presence of modulations in the lattice constant of the quaternary alloy sample. These were interpreted as possibly due to some tendency toward long-range ordering in the crystal. An intensive investigation was carried out in an effort to see whether or not a definite determination could be made.

Very high sensitivity step scans (using quartz crystal monochomatized $MoK_a$ radiation) were taken through the background between the Bragg peaks along the reciprocal lattice lines 000-0h0, 000-h̄h0, and 000-hhh. Stability of the radiation source was sufficient to ensure reproducible output over a time period of many weeks. Care was taken to eliminate fractional

Table 2. Room Temperature Photoluminescence Peak Widths

| Sample | Bandgap (eV) | FWHM (meV) | Mismatch (%) |
|---|---|---|---|
| 2-021 | 0.99 | 90 | * |
| 2-022 | 0.99 | 73 | -0.06 |
| 2-024 | 0.91 | 82 | * |
| 2-031 | 0.89 | 64 | * |
| 2-035 | 0.87 | 54 | * |
| 2-040 | 0.77 | 105 | -0.03 |
| 2-045 | 0.86 | 54 | 0.24 |
| 5-015 | 0.81 | 90 | 0.26 |
| 5-017 | 0.86 | 60 | 0.24 |
| 5-027 | 0.74 | 94 | 0.30 |

*Mismatch < ±0.03%

wavelengths from the monochromator by properly adjusting the pulse height analyzer. Operating parameters are listed in Table 3, and diffraction patterns are shown in Figures 4 through 7. Approximately three minutes were spent collecting counts for each angular increment shown.

Generally, diffraction pattern backgrounds were higher in all directions of the recpirocal lattice in the quaternary crystal than they were in that for the InP crystal substrate. However, as reported previously, the quaternary alloy yielded a number of well-defined but weak Bragg peaks where the intensities were three or more orders of magnitude below the principal Bragg peak intensity. Weak reflections not permitted in the zinc blende structure were observed to be as follows: (110), $\frac{1}{2}$(111), $\frac{1}{2}$(500), $\frac{1}{2}$(550), (330). It was concluded that these were not induced by fractional wavelengths since not only was the possibility of having fractional wavelengths eliminated by use of a carefully adjusted pulse height analyzer but also the excitation potential was selected so as to locate $\lambda/2$ at the cut-off wavelength of the continuous spectrum. Furthermore, the absence of extra reflections in a control crystal of InP verified the absence of fractional wavelengths. Any possible double reflection resulting from combining two existing reflections was excluded by the extinction rule for zinc blende structure where $h + k$, $k + \ell$, $(\ell + h) = 2 n$ for $(hk\ell)$ must be satisfied. Thus it was concluded that the extra peaks seen were due to the presence of some structure present in the Q1-72 quaternary crystal in addition to the normal zinc blende structure. Following these observations, a variety of crystal structures was systematically examined to see whether or not the extra lines could be explained by any other structure.

Speaking in general terms, long-range ordering results in a derivative structure from the basic structure with a set of equipoints being divided into two or more subgroups (with an increase of unit cell size if necessary).

18

Table 3. Diffractometer Operating Parameters for 2-θ Scan

| | Continuous Scan | Step Scan |
|---|---|---|
| X-ray radiation | $MoK_\beta$ | $MoK_\alpha$ |
| Wavelength | 0.6322 Å | 0.7107 Å |
| Operating voltage | 36 kV | 36 kV |
| Operating current | 16 mA | 16 mA |
| X-ray tube takeoff angle | 1.2° | 1.2° |
| Filtering arrangement | Unbent quartz crystal monochromator, 10Ī1 plane | |
| Scan speed | 2°/min | |
| Strip chart speed | 0.25 in/min | |
| Detector type | Scintillation counter | |
| Detector voltage | 1 kV | 1 kV |
| Pulse height analyzer setting | Upper level: 0.8 keV | |
| | Lower level: 0.4 keV | |

19
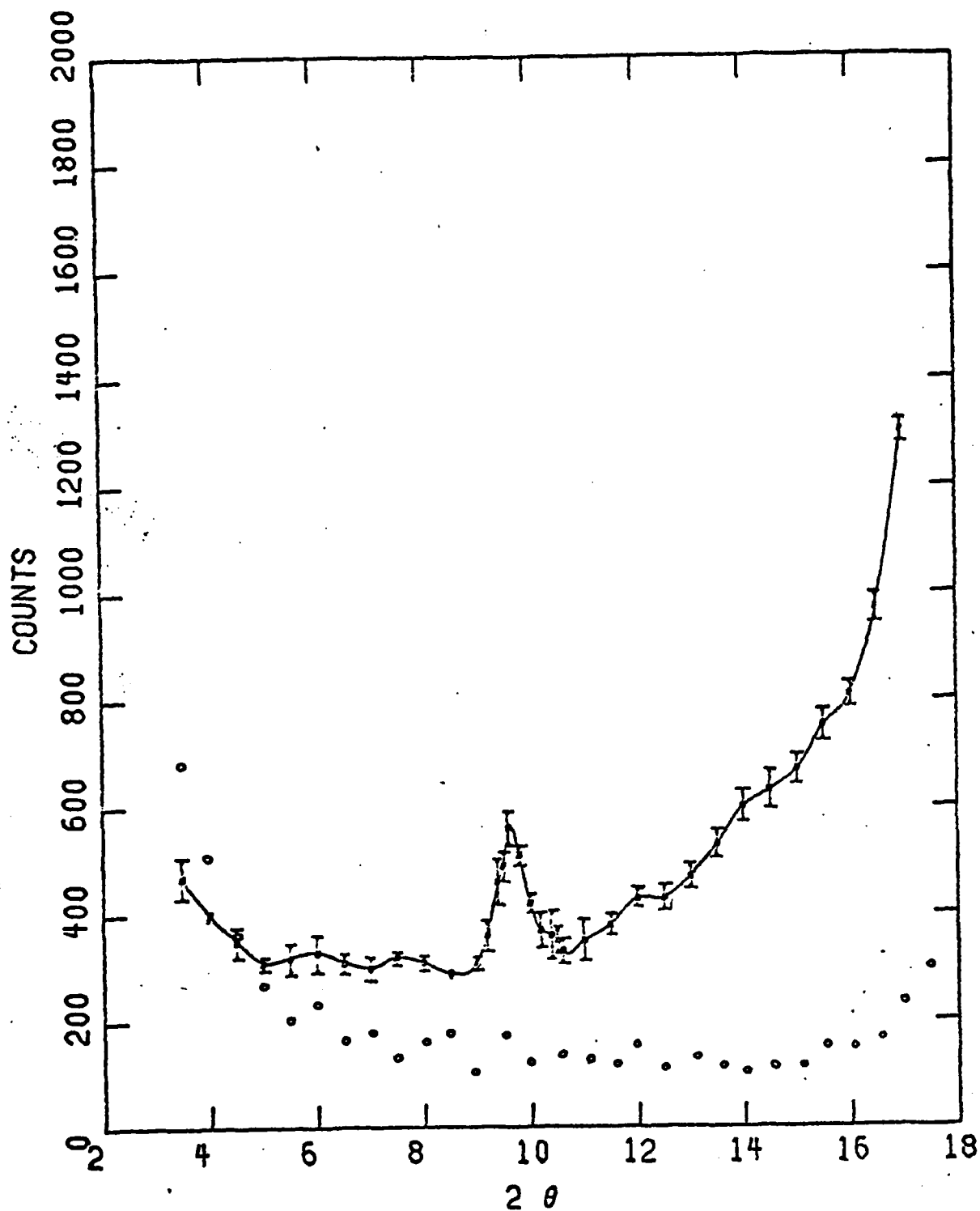
Figure 4. 2Θ-Step scan pattern showing extra reflection ($\bar{1}10$).
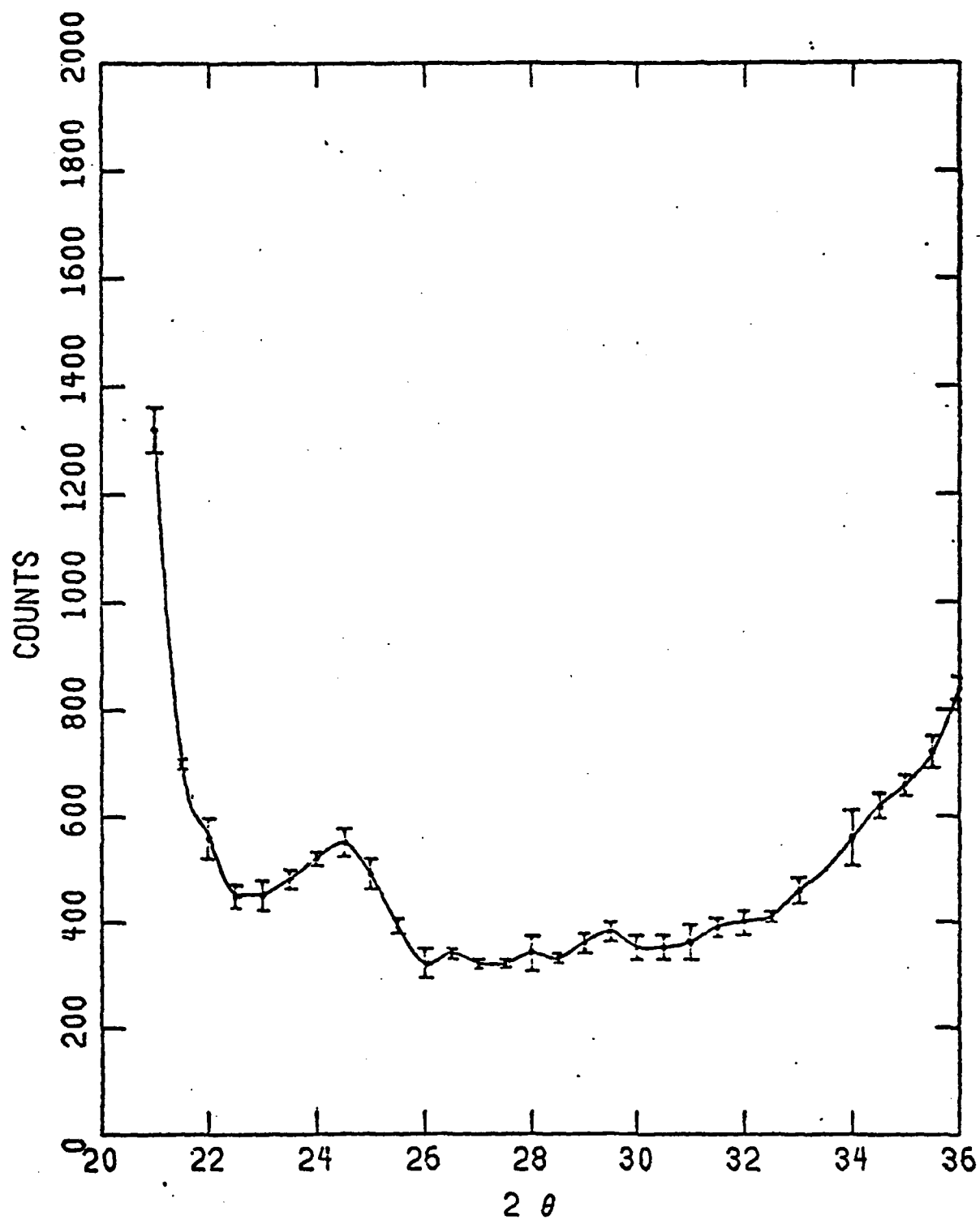
Figure 5. 2θ-Step scan pattern showing extra reflections ½ ($\bar{5}$50), ($\bar{3}$30).

21
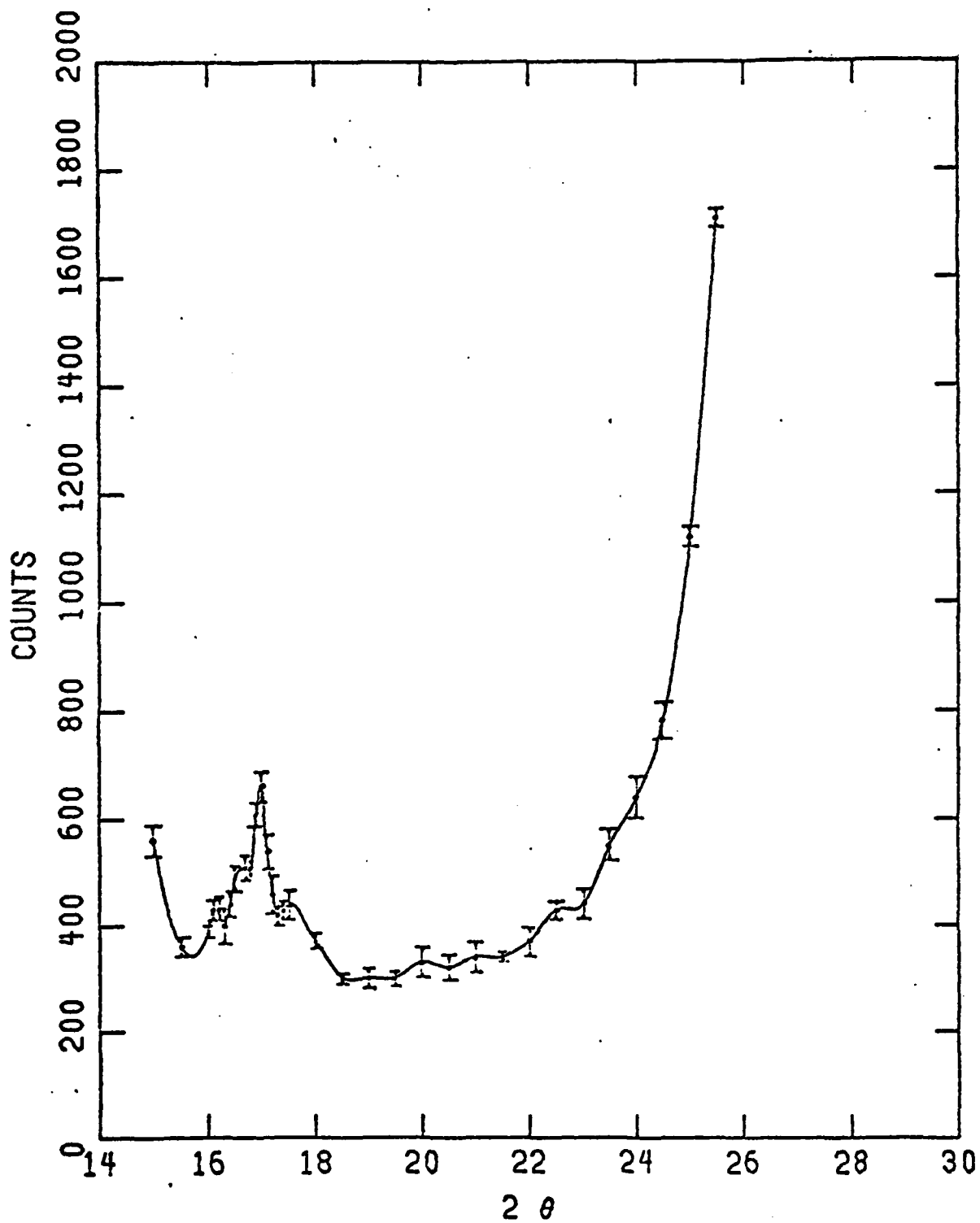
Figure 6.   2θ-Step scan pattern showing extra reflection ½ (050).

22
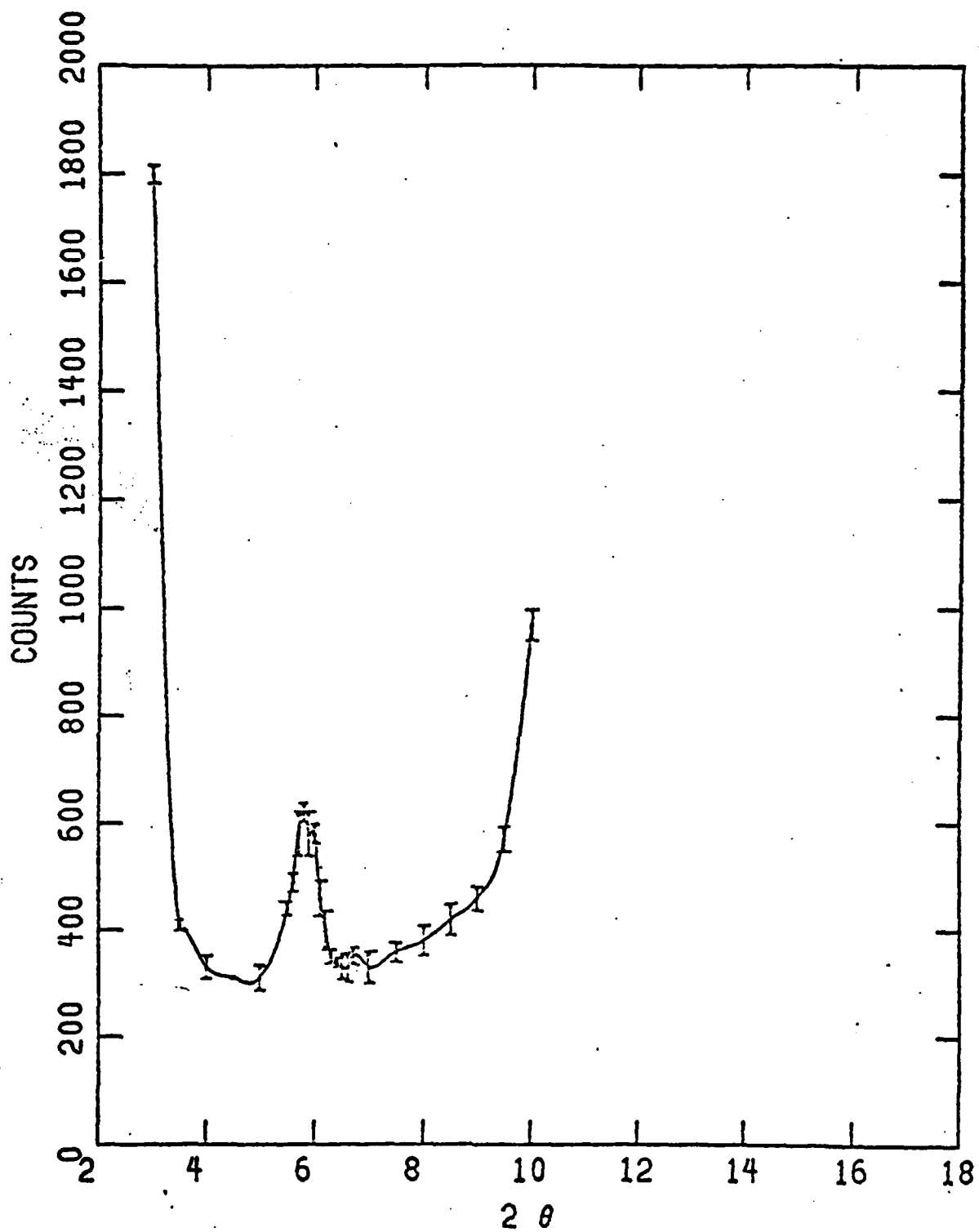
Figure 7.  2θ-Step scan pattern showing extra reflection ½ (1$\bar{1}$1).

The zinc blende structure, which is the basic structure of the derived superlattice, belongs to the cubic system. To check crystal symmetry, equivalent reflections $\bar{1}10$, $\bar{1}01$, and $01\bar{1}$ were chosen for their identical absorption corrections. Three peaks of identical shape and size were observed as shown in Figures 4, 8, and 9, showing that (111) is a threefold axis and leading to the conclusion that the structure is either cubic or rhombohedral.

By doubling the edge length of the unit cell, the observed superstructure reflections could be indexed properly and become 220, 111, 500, 550, and 660 of the larger cell. Thus it was concluded that there is a distinct possibility of long-range ordering on the anion or cation sublattice, or on both. Further, it can be concluded that the cubic unit cell of such a superlattice contains 64 atoms rather than eight and that the unit cell has a lattice constant twice that of the host lattice.

Since the coordinates for all the atoms in the unit cell are known, the usual search for the possible space groups implied by "diffraction symbol" through determining conditions for a set of possible reflections is unnecessary and time consuming. A survey of the 36 possible cubic space groups capable of allowing correct placement of cations and anions determined that the possible space groups are limited to the following: P23, P213, F23, I23, and P$\bar{4}$3n. Coordinates for the special and general positions of each of the equipoints are listed in Table 4. The observed superstructure reflections 111, 200, 500, 550, and 660 satisfy only space group P23 and none of the others.

Further discussion of structural possibilities is provided in Appendix A.

24
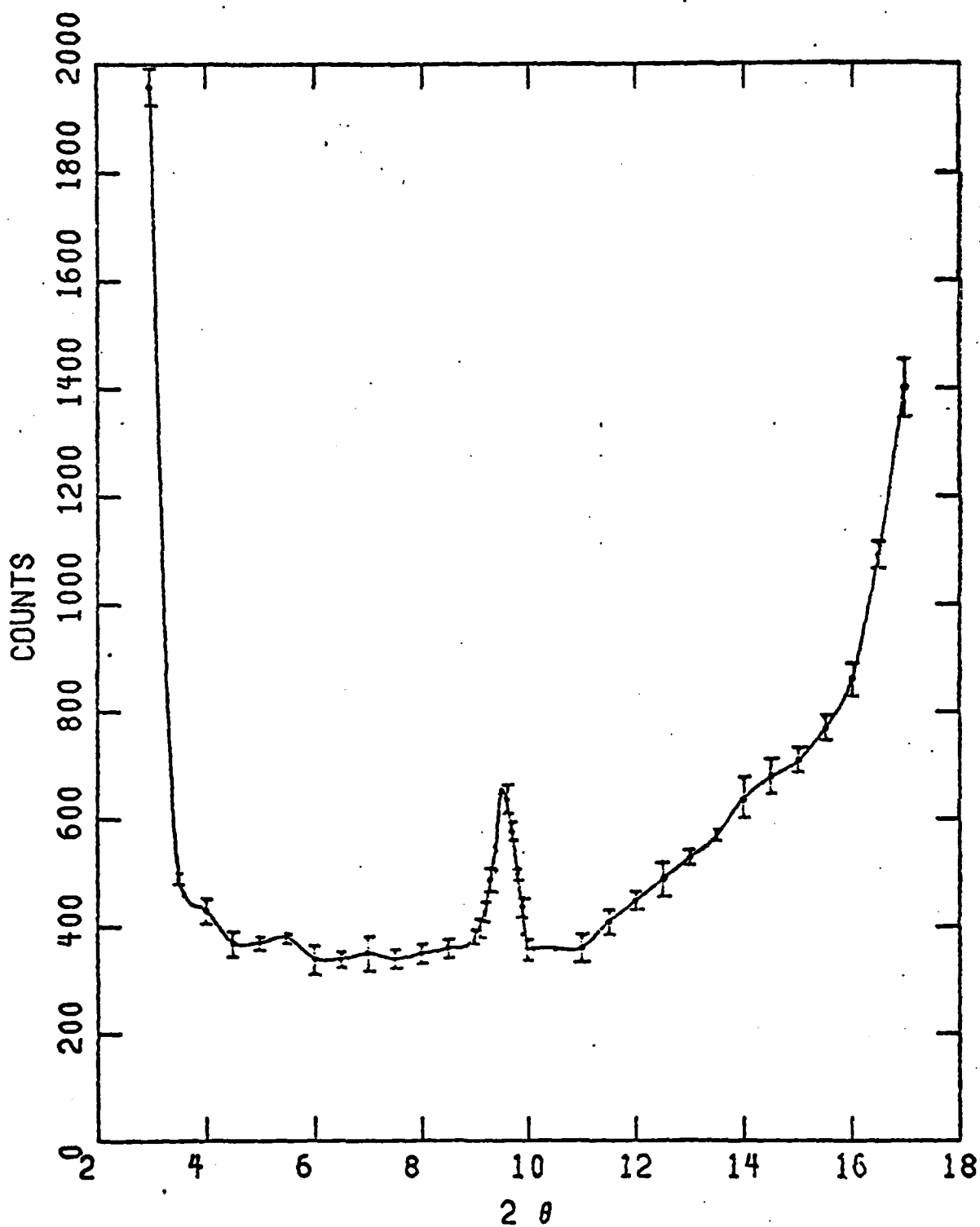
Figure 8.   2θ-Step scan pattern showing extra reflection (1̄01).

25
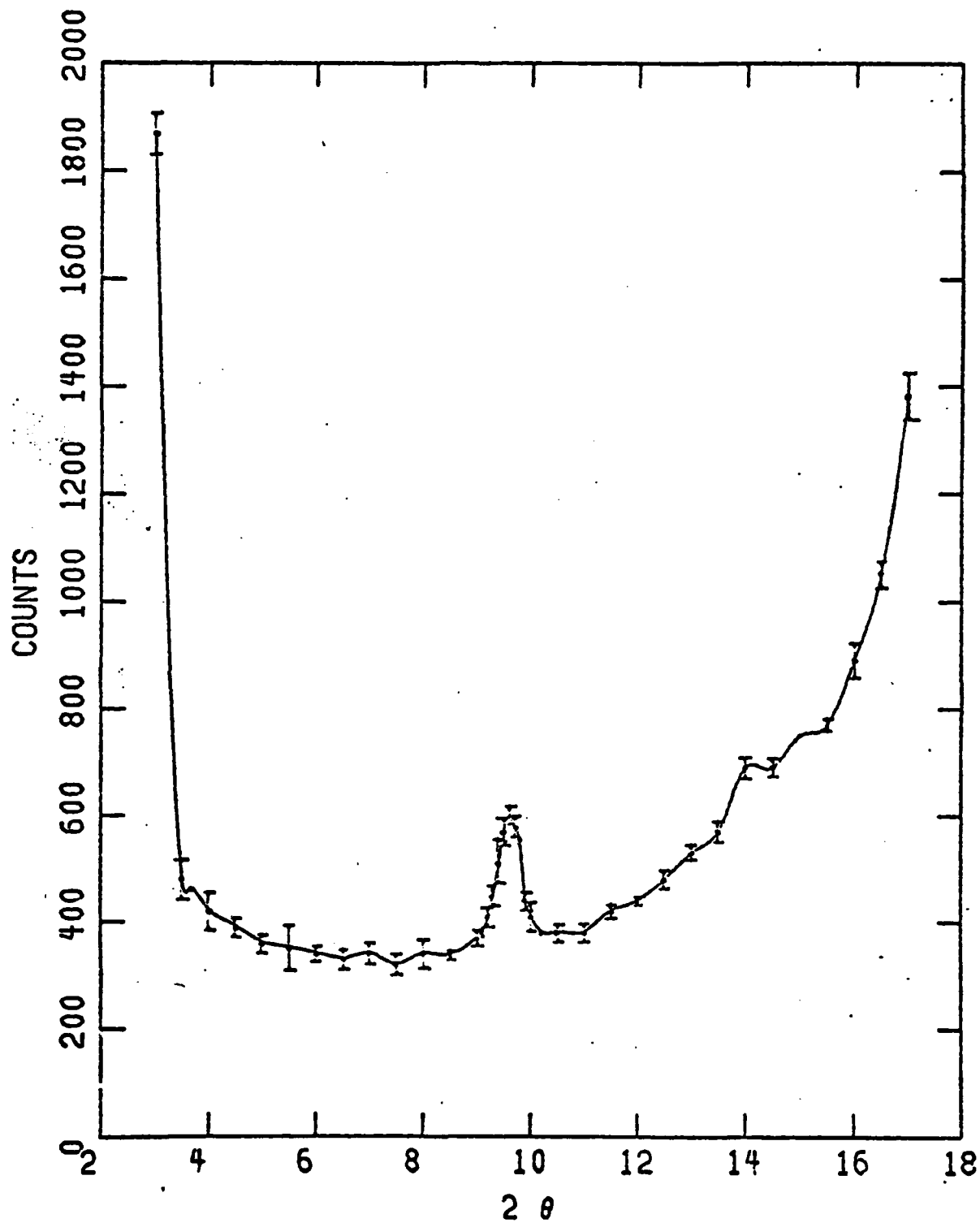
Figure 9. 2θ-Step scan pattern showing extra reflection (01$\bar{1}$).

Table 4. Possible Space Groups for Cubic Structure Model

| Space Group | A | | B | |
|---|---|---|---|---|
| **#195** **P23** | | | | |
| 1 (a) | 000 | | | |
| 1 (b) | ½½½ | | | |
| 3 (c) | 0½½   ½0½   ½½0 | | | |
| 3 (d) | ½00   0½0   00½ | | | |
| 12 (j) | (x=¼,  y=⅓,  z=0) | | 4 (e) | (x=⅛)  xxx |
| | xyz   zxy   yzx | | 4 (e) | (x=⅝)  x̄x̄x |
| | x̄ȳz   z̄x̄y   yz̄x̄ | | 12 (j) | (x=⅛,  y=⅛,  z=⅝) |
| | x̄yz̄   z̄xȳ   ȳz̄x | | | x̄x̄x   xx̄x̄   x̄xx̄ |
| | xȳz̄   zx̄ȳ   ȳzx̄ | | | |
| 12 (j) | (x=¼,  y=¼,  z=½) | | 12 (j) | (x=⅜,  y=⅜,  z=⅛) |
| | | | | x̄x̄x   xx̄x̄   x̄xx̄ |
| **#196** **. F23** | (000,  0½½,  ½0½,  ½½0) + | | | |
| 4 (a) | 000 | | 16 (e) | (x=⅛) |
| 4 (b) | ½½½ | | | xxx |
| 24 (g) | (x=0) | | 16 (e) | (x=⅝) |
| | x¼¼   ¼¼x   ¼¼x̄ | | | x̄x̄x   xx̄x̄   x̄xx̄ |
| | x̄¼¾   ¾x¼   ¾¼x̄ | | | |

Table 4 Continued

| Space Group | A | B |
|---|---|---|
| **#197 I23** | $(000, \tfrac{1}{2}\tfrac{1}{2}\tfrac{1}{2})+$ | |
| 2 (a) | 000 | 8 (c) $(x=\tfrac{1}{8})$ |
| 6 (b) | $0\tfrac{1}{2}\tfrac{1}{2}$  $\tfrac{1}{2}0\tfrac{1}{2}$  $\tfrac{1}{2}\tfrac{1}{2}0$ | $xxx$ |
| 24 (f) | $(x=\tfrac{1}{4},\ y=\tfrac{1}{4},\ x=0)$ | 24 (f) $(x=\tfrac{3}{8},\ y=\tfrac{3}{8},\ z=\tfrac{1}{8})$ |
| | $xyz$  $zxy$  $yzx$ | $xxx$  $\bar{x}\bar{x}x$  $\bar{x}\bar{x}\bar{x}$ |
| | $\bar{x}\bar{y}z$  $z\bar{x}\bar{y}$  $y\bar{z}\bar{x}$ | $\bar{x}\bar{x}x$  $\bar{x}xx$  $x\bar{x}\bar{x}$ |
| | $\bar{x}y\bar{z}$  $\bar{z}x\bar{y}$  $\bar{y}z\bar{x}$ | |
| | $x\bar{y}\bar{z}$  $\bar{z}\bar{x}y$  $\bar{y}\bar{z}x$ | |
| **#198 P2$_1$3** | 4 (a) $(x=0)$ | 4 (a) $(x=\tfrac{1}{8})$ |
| | $xxx$  $\tfrac{1}{2}+x,\tfrac{1}{2}-x,\bar{x}$ | |
| | $-x,\tfrac{1}{2}+x,\tfrac{1}{2}-x$  $\tfrac{1}{2}-x,\bar{x},\tfrac{1}{2}+x$ | |
| | 4 (a) $(x=\tfrac{1}{2})$ | 4 (a) $(x=\tfrac{5}{8})$ |
| | 12 (b) $(x=\tfrac{1}{4},\ y=\tfrac{1}{4},\ z=0)$ | 12 (b) $(x=\tfrac{5}{8},\ y=\tfrac{1}{8},\ z=\tfrac{1}{8})$ |
| | $\tfrac{1}{2}+x,\tfrac{1}{2}-y,\bar{z}$  $\tfrac{1}{2}+z,\tfrac{1}{2}-x,\bar{y}$  $\tfrac{1}{2}+y,\tfrac{1}{2}-z,\bar{x}$  $xyz$ | |
| | $\bar{x},\tfrac{1}{2}+y,\tfrac{1}{2}-z$  $\bar{z},\tfrac{1}{2}+x,\tfrac{1}{2}-y$  $\bar{y},\tfrac{1}{2}+z,\tfrac{1}{2}-x$  $zxy$ | |
| | $\tfrac{1}{2}-x,\bar{y},\tfrac{1}{2}+z$  $\tfrac{1}{2}-z,\bar{x},\tfrac{1}{2}+y$  $\tfrac{1}{2}-y,\bar{z},\tfrac{1}{2}+x$  $yzx$ | |
| | 12 (b) $(x=\tfrac{3}{4},\ y=0,\ z=\tfrac{1}{4})$ | 12 (b) $(x=\tfrac{3}{8},\ y=\tfrac{3}{8},\ z=\tfrac{1}{8})$ |

28

Table 4 Continued

| Space Group | A | | | B | |
|---|---|---|---|---|---|
| #218 | | | | | |
| Pḡ3n | | | | | |
| 2 (a) | 000 | ½½½ | | | |
| 6 (b) | 0½½ | ½½0 | | | |
| | ½0½ | | | | |
| | ½00 | 00½ | | | |
| 24 (i) | (x=¼, y=¼, z=0) | | | 8 (e) | (x=⅛) |
| | xyz | zxy | yzx | xxx | ½+x, ½+x, ½+x |
| | x̄ȳz | z̄xȳ | ȳz̄x | x̄x̄x | ½+x, ½−x, ½−x |
| | x̄yz̄ | z̄x̄y | yz̄x̄ | x̄x̄x̄ | ½−x, ½+x, ½−x |
| | xȳz̄ | zx̄ȳ | ȳzx̄ | x̄x̄x | ½−x, ½−x, ½+x |
| | | | | 24 (i) | (x=³⁄₈, y=³⁄₈, z=⅛) |
| | ½+x, ½+y, ½+z | ½+y, ½+x, ½+z | | | |
| | ½+z, ½+x, ½+y | ½+x, ½+z, ½+y | | | |
| | ½+y, ½+z, ½−x | ½+z, ½+y, ½−x | | | |
| | ½−x, ½+y, ½−z | ½−y, ½+x, ½−z | | | |
| | ½−z, ½+y, ½−x | ½−x, ½−z, ½−y | | | |
| | ½−y, ½−x, ½+z | ½−y, ½−z, ½+x | | | |

At this point the existence of long-range order has not been unequivo-
cally established. In fact, as discussed in Section 5, there is evidence
that at least some of the quaternary alloy samples prepared in this
research, if not all, have considerable defects, the nature of which has
yet to be determined.

## 3.2  Electrical Properties

Hall effect measurements were made using the standard Van der Pauw
method to determine Hall mobility and net carrier concentration. For
unintentionally doped layers, the net electron concentration due to back-
ground impurities is found to be in the low $10^{16}$ $cm^{-3}$ range. A summary of
these measurements is given in Table 5. For higher doping density, three
donor impurities—Sn, Te, and Se—have been used successfully. All three
are well behaved, shallow donors in this quaternary with a doping behavior
similar to that in InP but with slightly different distribution coefficients,
as discussed previously in Section 2.3.

Table 5.  Carrier Concentrations and Electron Mobility Values
at 300 K and 77 K for Quaternary Alloy Samples

| Sample | $n(\times 10^{-17} cm^{-3})$ | | $\mu_n (cm^2/V\text{-}s)$ | |
|---|---|---|---|---|
| | 300 K | 77 K | 300 K | 77 K |
| 2-022 | 2.75 | --- | 2248 | --- |
| 2-024 | 0.114 | 0.132 | 2282 | 4990 |
| 2-025 | 0.103 | --- | 1952 | --- |
| 2-032 | 0.762 | 0.734 | 3174 | 4295 |
| 2-035 | 3.43 | 3.16 | 3074 | 4086 |
| 5-010 | 0.483 | --- | 1368 | --- |
| 5-026 | 1.64 | --- | 2071 | --- |

Using the form

$$\frac{\mu(T_1)}{\mu(T_2)} = \left(\frac{T_1}{T_2}\right)^b , \qquad\qquad (1)$$

the samples for which 300 K and 77 K data are reported in Table 5 show a temperature dependence which ranges from b = -0.21 to b = -0.58. As expected, this is a definite correlation between the carrier concentration and the reduction in mobility.

Theoretical calculations of electron mobility values in $Ga_{1-x}In_xP_{1-y}As_y$ alloys using Monte Carlo techniques have been made for those alloy compositions which are lattice matched to InP [6]. The theoretically predicted variation of Hall mobility is shown in Figure 10 compared to the range of values obtained experimentally [14,15]. Efforts to achieve a better fit of theory to experiment [16] have had to invoke relatively large amounts of compensation by acceptor impurities to increase the contribution of ionized impurity scattering as well as large amounts of "alloy" scattering. The latter has been treated theoretically by several approaches [17] which give a $T^{1/2}$ dependence—namely, so-called "space-charge scattering" [18,19]—which acts to decrease the mobility below that predicted for III-V compound alloys when the mechanisms of polar optical mode, ionized impurity, and alloy scattering are invoked.

Figures 11 and 12 show data points derived from Hall effect and conductivity measurements by Houston and his co-workers [20] on two $Ga_{1-x}In_xP_{1-y}As_y$ alloy samples grown by standard liquid phase epitaxy techniques in our laboratory. These layers were grown on iron-doped InP substrates and are both almost exactly lattice matched to InP. The Hall mobility for both samples rises to a maximum at about 100 K in both cases

31
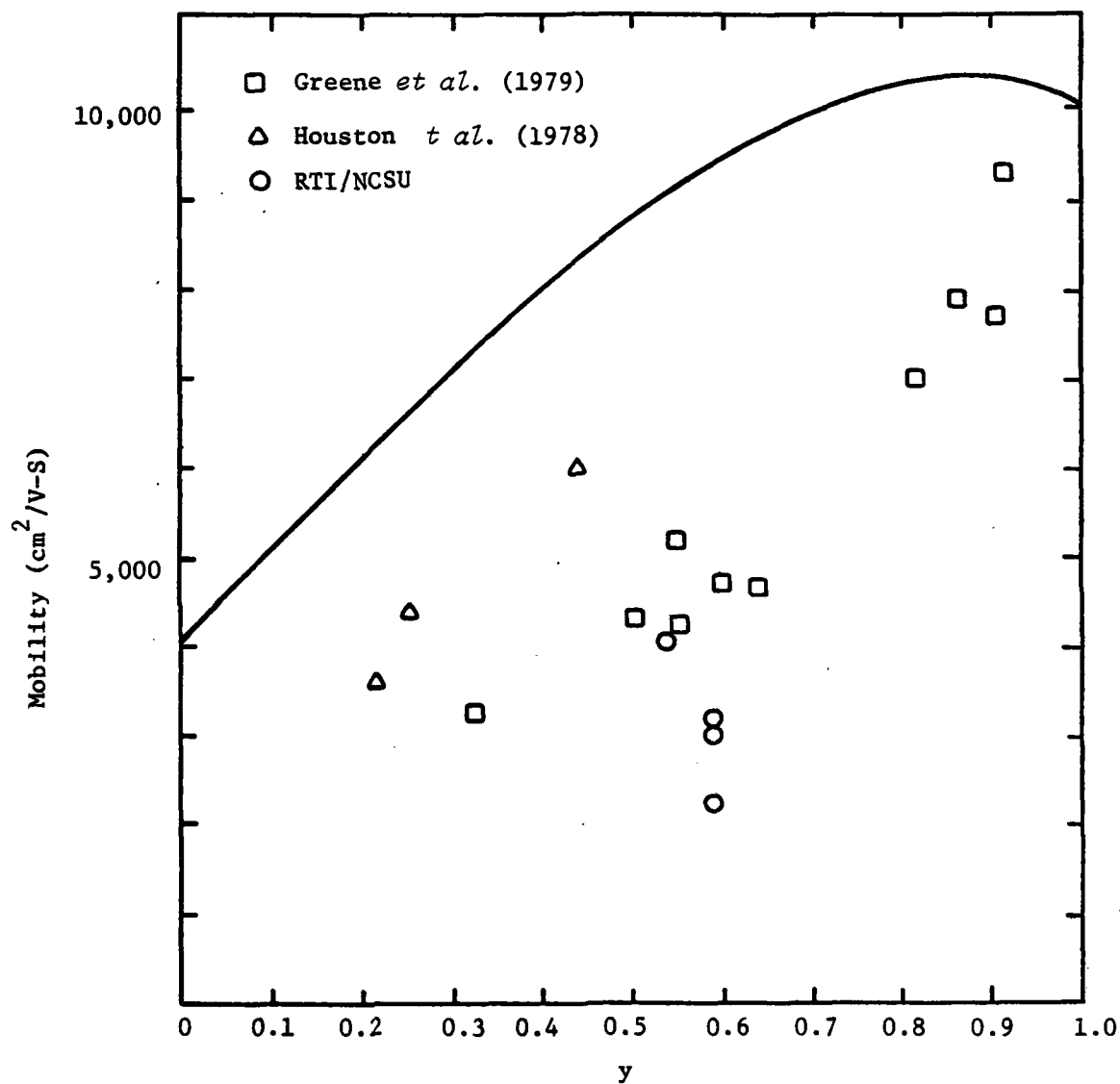
Figure 10. Comparison of theoretical and experimental values for electron mobility in $Ga_{1-x}In_xP_{1-y}As_y$ epitaxial layers lattice matched to InP.
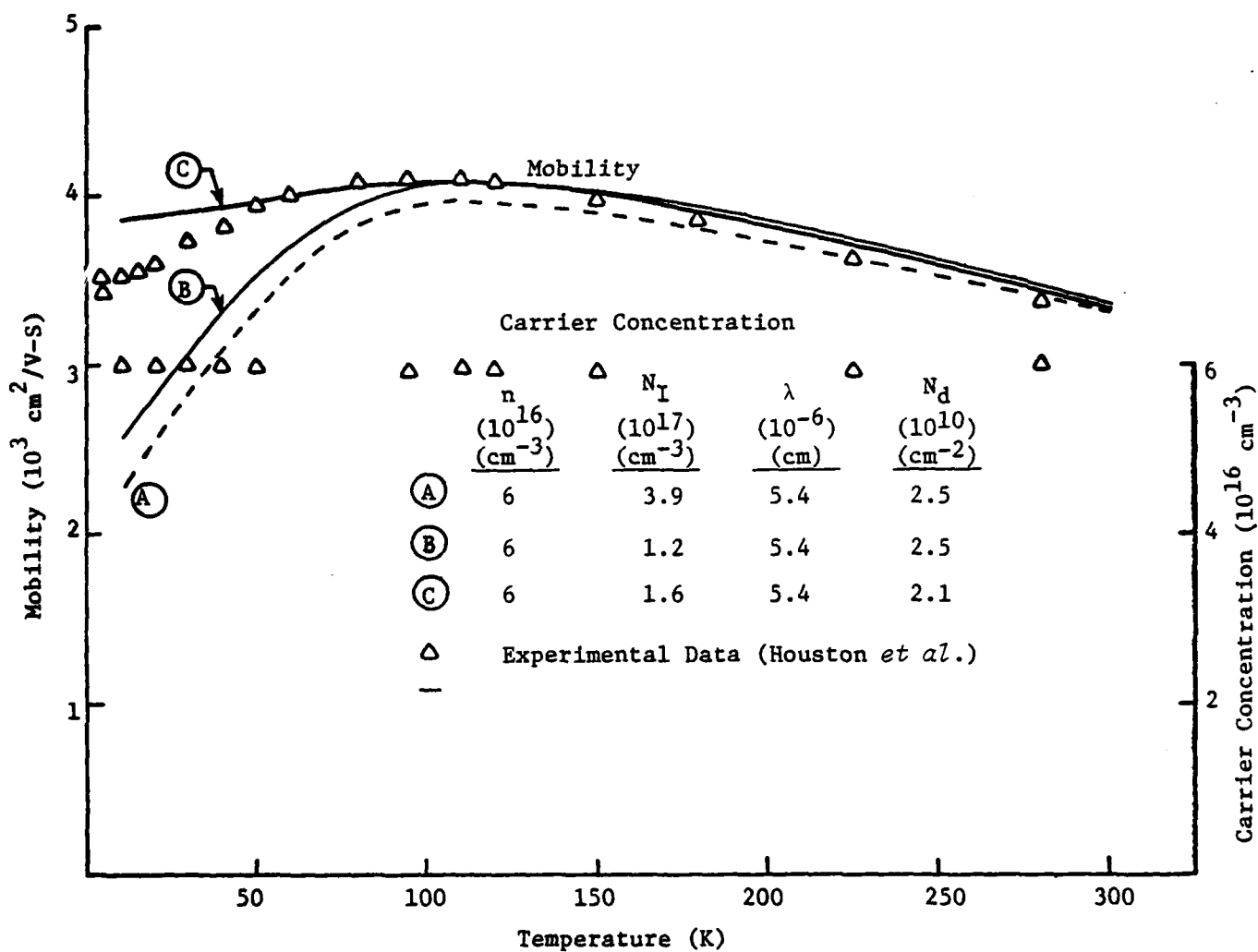
Figure 11. Comparison of calculated and experimental values for electron mobility *vs*. temperature for $Ga_{0.31}In_{0.69}P_{0.36}As_{0.64}$ alloy epitaxial layer.
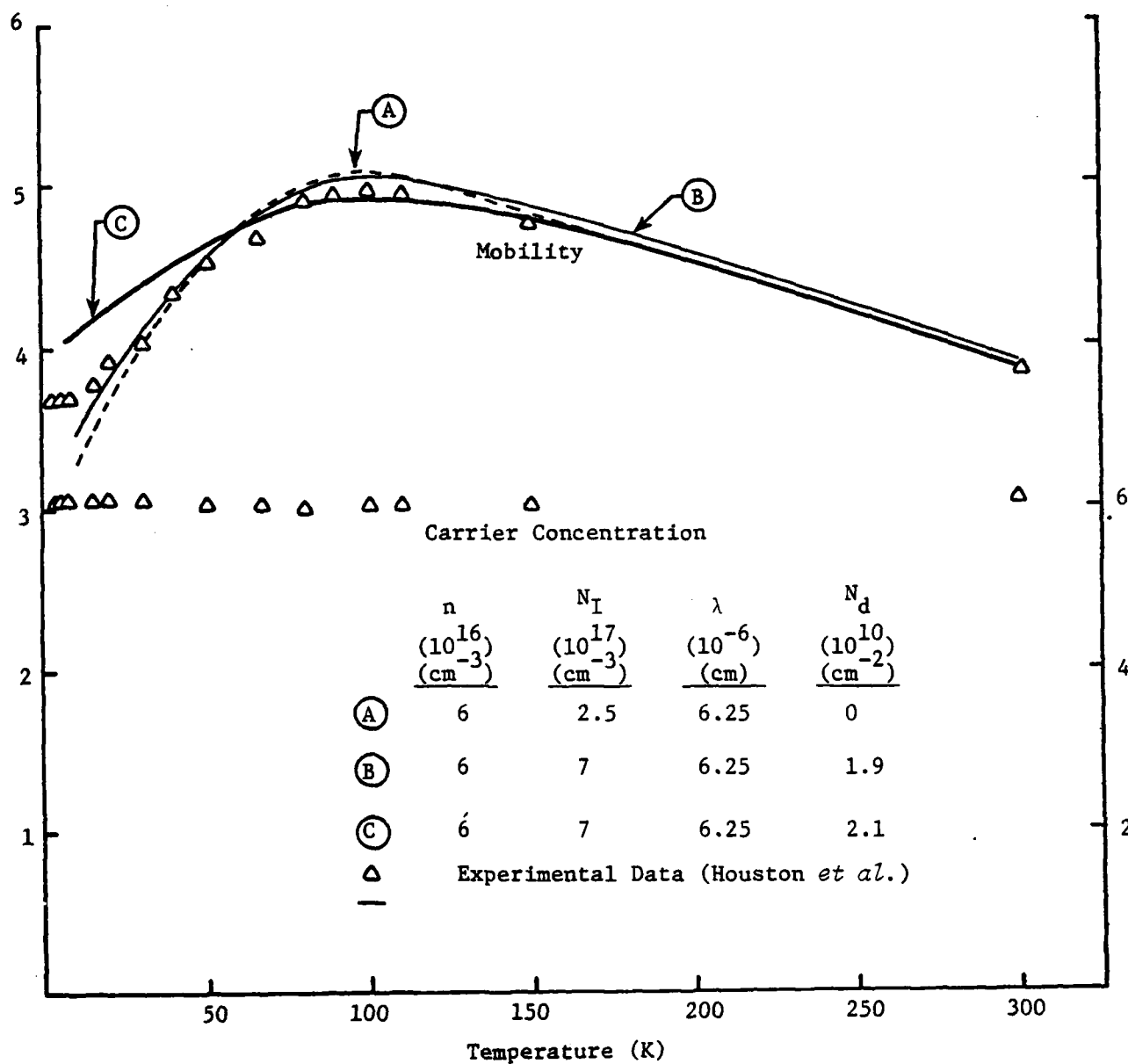
**Figure 12.** Comparison of calculated and experimental values for electron mobility *vs.* temperature for $Ga_{0.27}In_{0.73}P_{0.42}As_{0.58}$ alloy epitaxial layer.

and then decreases to a saturating value at temperatures below about 10 to 20 K. The latter, of course, is explicable in terms of impurity band conduction [21]. The shape of the experimental curves in Figures 11 and 12 may be explained by the combination of polar optical mode, ionized impurity, and alloy/space charge scattering alone or by invoking an additional mechanism, dislocation scattering [22]. A reasonable fit to the experimental curves is obtained by using a simple extension of the models used for ternary alloys [23] and adapting the Dexter and Seitz [22] formula,

$$\frac{1}{\mu_{DS}} = 3.05 \times 10^3 \; E_1^2 \lambda^2 \left(\frac{1 - 2\nu}{1 - \nu}\right)^2 \frac{N_d}{T} \left(\frac{m^*}{m_0}\right)\left(\frac{V - s}{cm^2}\right) \tag{2}$$

where $E_1$ is the deformation potential (eV), $\lambda$ is the crystallographic slip distance (cm), $\nu$ is the Poisson ratio for the material, $N_d$ is the number of dislocations per $cm^2$, and T is the temperature (K). $N_d$ was treated as an adjustable parameter, and estimates were used for the other parameters as follows: $E_1 = 6.0$ eV, $\lambda = 2.5 \times 10^{-8}$ cm, and $\nu = 0.3$.

Weisberg's formula [19] for space charge mobility was used in the form

$$\frac{1}{\mu_W} = 4.7 \times 10^{-10} \left(\frac{m^*}{m_0}\right)^{1/2} \frac{T^{1/2}}{\lambda} \left(\frac{V - s}{cm^2}\right) \tag{3}$$

where the parameter $\lambda$ (in cm) is the mean free path for scattering by large cross section objects (opaque scattering centers) whose cross section is taken in this treatment to be independent of temperature. This mean free path is equal to the product of $N_S$, the number of opaque scattering centers per unit volume, and $A_S$, the cross-sectional area of the scattering center. More properly,

$$\lambda^{-1} = N_S \cdot A_S = \sum_{k=1}^{N_S} A_{Sk} \qquad (4)$$

where

$$A_S = \frac{1}{N_S} \sum_{k=1}^{N_S} A_{Sk} \qquad (5)$$

and $A_{Sk}$ represents the cross-sectional area for electron scattering for the $k^{th}$ object in the unit volume.

Fermi-Dirac integrals were used to calculate energy averages for the mobility and scattering factors for each mechanism. For Curves A and B for each sample the effect of degeneracy on the screening radius for ionized impurity scattering has been taken into account [24].

Combination of reciprocal mobilities for the various scattering mechanisms is used to calculate a conductivity mobility. This is then corrected by an average scattering factor calculated from

$$\bar{r} = \frac{\sum\limits_{k} r_k <1/\tau_k>}{\sum\limits_{k} <1/\tau_k>} \qquad (6)$$

to obtain the Hall mobility,

$$\mu_H = \frac{\bar{r}}{\sum\limits_{k} \frac{1}{\mu_k}} \qquad (7)$$

As can be seen from Figures 11 and 12, good fits are obtained in the temperature range 50 to 300 K for reasonable values of the parameters.

For both samples $\lambda \sim 6.0 \times 10^{-6}$ cm. If an average diameter of 50 Å is assumed, $N_S \sim 8 \times 10^{17}$ cm$^{-3}$. In this case approximately one half of

the volume would be occupied by the hypothetical opaque scattering centers. Since the fraction of volume occupied by the (assumed spherical) opaque scattering centers is given by

$$f_S = \frac{16}{3} d_S / \lambda , \qquad\qquad (8)$$

reduction of the diameter, $d_S$, to 10 $\overset{\circ}{A}$ would reduce the volume fraction, $f_S$, to about 9 percent.

If the opaque scattering centers occupied an appreciable fraction of the volume of the alloy and were of different crystal structure, one would expect detection by X-ray diffraction. However, our X-ray diffraction measurements of similar $Ga_{1-x}In_xP_{1-y}As_y$ alloy samples prepared in our laboratories have not revealed the presence of any lines that could be interpreted as the existence of a separate phase as inclusions (e.g., indium). As discussed previously in Section 3.1, extra lines do appear [25], but these exhibit the same symmetry as the host lattice with an apparent doubling of the lattice constant. Therefore, either the volume fraction is small enough to reduce diffraction lines down to the noise level, or the opaque scattering centers have essentially the same symmetry properties as the host lattice.

Since there is some controversy [17] about the proper choice for the scattering potential used in the calculation of alloy scattering, use of differences in energy bandgap values rather than either electron affinity differences or electronegativity differences was examined. This would increase the alloy scattering rate by a factor of about three whereas an increase by a factor of about 24 is required to explain the difference necessary to fit the experimental data.

37

There is evidence that the effects producing the shape of the mobility curves for the $Ga_{1-x}In_xP_{1-y}As_y$ are caused by some mechanism other than alloy scattering per se. Figure 2 in Reference 26 displays a plot of electron mobility versus temperature for vapor phase epitaxial InP samples. One of these samples, CV66, with a nominal electron concentration of $3.5 \times 10^{17}$ $cm^{-3}$ at 300 K, has a curve shape similar to those for the alloy sample shown in Figures 11 and 12 of this report. Similarly, Figure 3 in Reference 27 displays a plot of mobility versus temperature for samples of GaAs obtained commercially ca 1970 (presumably either Czochralski or Bridgman process growth). Two of these curves have shapes similar to those for the alloy samples in Figures 11 and 12.

In summary, for many materials with moderate values of electron concentration ($\sim 10^{16}$ to $10^{17}$ $cm^{-3}$), there appears to be a mechanism present that contributes a component of scattering in the range 100 to 300 K at a rate proportional to $T^{1/2}$. In alloys, this process is indistinguishable from so-called alloy scattering except for those cases in which the magnitude of the $T^{1/2}$ component of scattering considerably exceeds that calculated from the simple theory for alloy scattering.

In the range of about 50 to 100 K the mobility in the samples shown in Figures 11 and 12 appears to be controlled either by ionized impurity scattering or by a combination of this with scattering from dislocations. The dislocation density calculated on the basis of Eq. (2) and the assumptions made concerning the parameter values used in this equation are in the range of $2 \times 10^{10}$ $cm^{-2}$. Both samples were almost exactly lattice matched to the InP substrates, and the substrates themselves had etch pit densities of about 6,000 $cm^{-2}$. Thus the existence of such a large dislocation density cannot be attributed to either of these factors. However, if the

opaque scattering centers invoked previously are due to the presence of a phase with a lattice constant sufficiently different from that of the host lattice, such high densities are plausible. Using a simple calculation [28], the lattice mismatch required to generate $2 \times 10^{10}$ dislocations per $cm^2$ is estimated at about 0.8 percent.

Based on the evidence presented, it appears that the electron mobility in $Ga_{1-x}In_xP_{1-y}As_y$ alloys grown by liquid phase epitaxy may be severely reduced by the presence of one or more phases that act both as opaque scattering centers and may in addition act as generators for dislocation networks. However, this phenomenon is also observed in InP grown by vapor phase epitaxy [26] and by bulk growth GaAs [27]. Since both of these binaries are also obtained with high quality and excellent electronic properties, it is concluded that there is considerable hope for improving the quality of $Ga_{1-x}In_xP_{1-y}As_y$ alloys.

## 4.0 DEVICE TECHNOLOGY

### 4.1 Contacts

Ohmic contacts to quaternary layers have been made using evaporated In or Au-Sn contacts with subsequent alloying at 400°C for three minutes in a hydrogen ambient.

For forming Schottky barriers, several metallization processes have been used--e.g., Au, Al, Cr, Ag, Mg. Thin layers ($\sim$1,000 $\overset{\circ}{A}$) of these metals were deposited on precleaned samples through a metal shadow mask with circular openings. Precleaning was done with a thorough rinse in organic solvents followed by a brief 15-second etch with 0.1-percent bromine-methanol solution with a final methanol rinse. After many trials, we have finally been able to get rectification with Au. Figure 13 shows a C-V plot for a 203-$\mu$m diameter metal dot. Here the barrier height is seen to be $\sim$0.51 V for a quaternary material bandgap of 0.96 eV ($\phi_B/E_g = 0.54$). In Figure 14 the forward I-V characteristic of this device is shown. From a straight line fit in the low current injection range, it is determined that $\phi_B = 0.51$ V and the diode factor n = 2.6.

Attempts have been made to make Schottky barriers on other quaternary samples with Au metal, but all these have proven to be unsuccessful. The reasons for this behavior are not yet fully understood. From all the experiments that have been performed in this period, no systematic trend for the occurrence of a rectifying barrier is evident. It is clear that more work is required in at least two areas: (1) in preparation of clean surfaces and (2) in structural evaluation of quaternary material for defect structures.
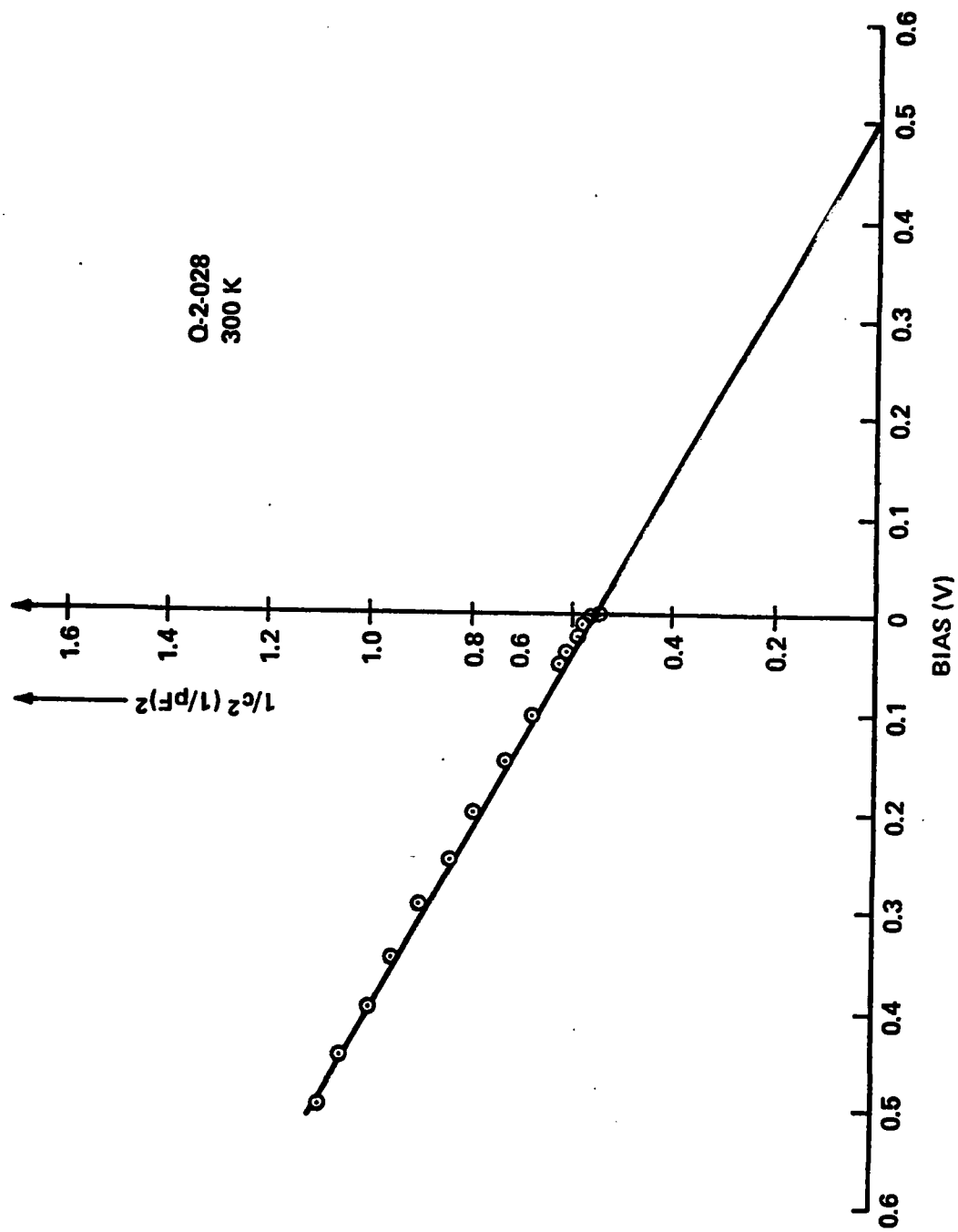
Figure 13. C-V curve for Au/n-GaInAsP Schottky barrier diode.

42
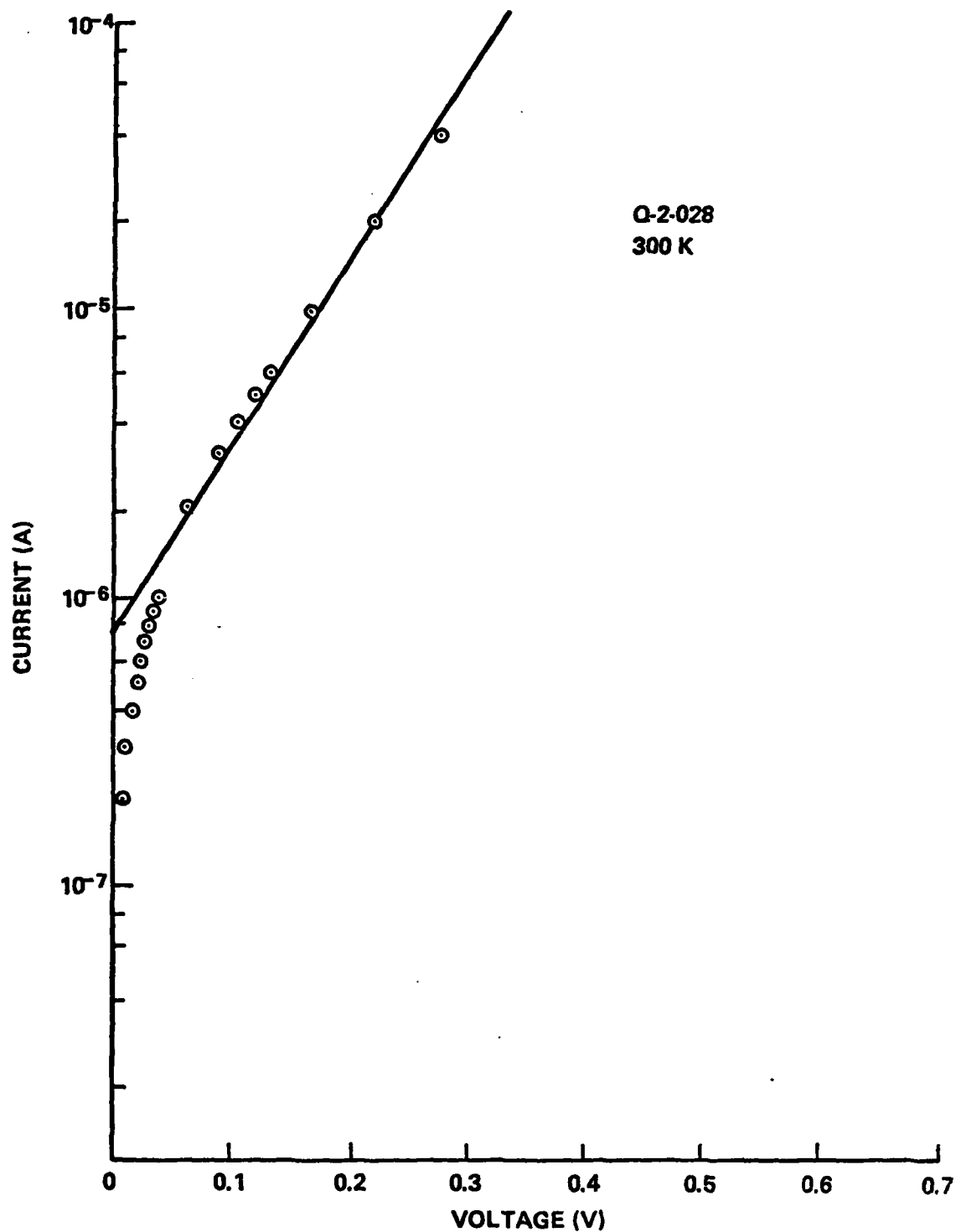
Figure 14.  Log I-V curve for forward characteristic of Schottky diode (same device as in Figure 4).

## 4.2 MESFET Design

Preliminary designs undertaken for MESFET devices optimized for X-band (8 to 12 GHz) and $K_a$-band (26 to 40 GHz) frequency ranges. Details are given in Appendix B. A summary of the calculated device DC parameters and figures of merit are given in Tables 6 and 7, respectively. It should be pointed out that these results were based on theoretical values for low field mobility and peak velocity [Ref. 6]. As reported previously, the values of low field mobility obtained to date have been about half that predicted theoretically. This and the problems cited in obtaining good Schottky barriers have prevented device fabrication to achieve the figure of merit values in Table 7.

Table 6. Device DC Parameters

|  | X-Band Device | $K_a$-Band Device |
|---|---|---|
| $I_{dss}$ (mA) | 427 | 136 |
| $I_{ds}$ (mA) | 64 | 20.5 |
| $V_{ds}$ (V) | 4 | 2 |
| $V_{pinch-off}$ (V) | 4.28 | 1.64 |

Table 7. Calculated Figures of Merit

|  | X-Band Device | $K_a$-Band Device |
|---|---|---|
| Cutoff frequency, $f_T$ | 23.9 GHz | 95.7 GHz |
| Max. frequency of oscillation, $f_{max}$ | 51.2 GHz | 165 GHz |
| Unilateral gain, U | 12.6 db at 12 GHz | 12.3 db at 40 GHz |

## 5.0 CONTRIBUTIONS AND COMMUNICATIONS

As a result of research done under this contract, the following scientific contributions were made possible:

1. S. B. Phatak and G. Kelner, "Material Selective Chemical Etching in the System InGaAsP/InP," J. Electrochem. Soc., 126:287 (1979).

2. B. Houston, J. B. Restorff, R. S. Allgaier, M. A. Littlejohn, and S. B. Phatak, "Shubnikov-de Hass Determination of Electron Effective Masses in InGaAsP," presented at APS Meeting, Chicago, Ill., March 1979.

3. M. A. Littlejohn, R. A. Sadler, T. H. Glisson, and J. R. Hauser, "Carrier Compensation and Alloy Scattering in $Ga_{1-x}In_xP_{1-y}As_y$ Grown by Liquid Phase Epitaxy," GaAs and Related Compounds, 1978 (Inst. Phys. Conf. Ser. No. 45), pp. 239-247.

4. Hsu, Juen, "Ordering in GaInPAs Crystals Grown by Liquid Phase Epitaxy," M.S. Thesis, 1979, North Carolina State University (unpublished).

5. J. W. Harrison, S. B. Phatak, M. A. Littlejohn, and B. Houston, "Comments on the Observation of Low Electron Mobility Values in $Ga_{1-x}In_xP_{1-y}As_y$ Alloys," to be submitted for publication.

APPENDIX A


Possible Superlattice Structures

J. Hsu

## I. CUBIC STRUCTURE MODELS AND STRUCTURE FACTOR CALCULATIONS

In order to determine the exact crystal structure of the super-lattice formed, it was necessary to set up various trial structure models, and then calculate the structure factors for each of these models. Actual observed structure factors were then compared with those of the models.

By combining the equipoints in different ways, and leaving out those that might be correlated by a simple translation, 452 arrangements compatible with the 273 hypothetical compositions are obtained. This is summarized below.

|     | Ratio Type | Permutation for Arrangements |
|-----|------------|------------------------------|
| 1   | aaaa       | 4                            |
| 27  | abcd       | 8 or 16                      |
| 11  | abcc       | 4 or 8 or 16                 |
| 3   | abab       | 8 or 16                      |

$$1 \times 4 + (13 \times 16 + 14 \times 8) + (2 \times 4 + 7 \times 8 + 2 \times 16)$$

$$+ (2 \times 8 + 1 \times 16) = 452 .$$

Since superlattices found in binary system are mostly in simple ratio, 132 structure models (having composition ratios up to 3:5:4:4) were set up, and structure factors were calculated for each model.

The computer program XFLS4 (May 1977 version) by Levy and Busing was used for structure factor calculation. This program is based on an

idea of calculating through symmetry operations and thus it may be applied to all space groups.

Structure factor for the ideal composition $Ga_3In_{13}P_2As_{14}$ (or $Ga_{0.19}In_{0.81}P_{0.13}As_{0.87}$) is also calculated, which is the nearest type to the experimental composition. The observed intensity ratio of super-structure to normal peaks tended to be lower. Due to the associated thermal and compositional disorder, it is unknown whether it might be fully ordered in this ratio, or whether it might be stable in some simpler ratio. Among the 132 structure models, some of the calculated structure factors for certain reflections are zero, although they have been observed in experiment. Where this is the case, these models may readily be excluded. Despite this, the possible number of arrangements still amounts to hundreds.

Based on these primary analyses, the diversified complexity of the ordering in this quaternary crystal is conceivable. It is thus proposed that further study first be limited to ternary systems. This would allow ordering to take place either in cation or in anion sub-lattice sites only, and the ordering then degenerates into a pseudo-binary case. In order to test the validity of this conclusion, two ternary compositions were step scanned, $Ga_{0.01}In_{0.99}As_{0.66}P_{0.34}$ (Q1-75) and $Ga_{0.47}In_{0.53}As$ (Q2-012) . (It should be pointed out to the reader that Q1-75 has only 0.01 percent Ga and may therefore be considered to be truly ternary.)

## II.  OTHER STRUCTURE MODELS

Since both  GaAs  and  InP  possess zinc blende structure, it
is expected that this quaternary compound has an adamantine (diamond-
like) structure (necessary conditions as electron rules summarized by
Parthé [29] are satisfied).  The adamantine structures form a subgroup
of the tetrahedral structures and show geometrical features of würtzite,
zinc blende, and related structures.

Parallel to the analysis based on zinc blende structure, vari-
ous würtzite derivative structures, known polytypes of  ZnS , CuPt
rhombohedral structure, and chalcopyrite structure, are tried out to
coincide with the observed superlattice reflections.  This is summar-
ized in Table 8.  The first three columns represent the experimental
reflections.  In the fourth column, the reflections that coincide with
those obtained by doubling the edge length of the original cell are
listed.  One can find the corresponding reflections by going horizon-
tally in the table.  When a hexagonal polytype is presumed, this can be
verified by a loss of cubic symmetry in the experimental crystal.  How-
ever, the possibility must be allowed that hexagonal "shifts" occur on
all four cubic {111} planes, which might restore an apparent cubic sym-
metry.  The same rationale can be used to invoke the tetragonal chalco-
pyrite type to explain extra reflections.  If the tetragonal c-axis
alternates between all three cube axes, the apparent symmetry of this
structure would be cubic.

A ternary case leading to a primitive cubic cell of the approximate size of GaAs would be obtained by having the two like ion species ordered in one sublattice as in $Cu_3Au$. From the known theory of that structure, it immediately follows that all primitive cubic reflections listed in the column below 3C in Table 8 should be observed. This is not compatible with the experimental observations, so that arrangement can be excluded from further discussion.

The rhombohedral CuPt type provides an ordering scheme that could explain the doubling of the cell edge of GaAs. The reflections due to this atomic arrangement are listed under CuPt II in Table 8. It cannot explain the observed reflections in the experimental crystals.

The orthorhombic $BeSiN_2$ structure type is derived from the hexagonal würtzite type by making $a = 2a_{hex}$, $b = \sqrt{3} \ a_{hex}$, $c = c_{hex}$ (referring to Parthé [29]). According to Table 8, it cannot account for all of the observed reflections in the three experimental crystals.

The well-known tetragonal chalcopyrite structure is obtained by doubling one cell edge of the cubic zinc blende type so that $a = a_{cubic}$ and $c = 2a_{cubic}$. It could explain some of the experimentally observed reflections, but does not account for the 111 and 550 reflections of the larger cubic cell with $a' = 2a_{GaAs}$.

Table 8. Bragg Reflections of Conventional GaAs Derivative Structure Coinciding with Primitive Cubic Reflections for a = 11.30

| Q1-72* Ga-In-P-As InP$_{0.34}$As$_{0.66}$ hkl | Q1-75 Ga$_{0.47}$In$_{0.53}$As hkl | Q2-012 hkl | Prim. Cubic a=11.30 hkl | d | 3C F.C. Cubic** a=5.65 hkl | Chalcopyrite Tetra. a=5.65 c=11.30 hkl | CuPt II Rhom. a=11.30 hkl | 2H Würtzite Hex a=3.99515 c=6.52405 hkl |
|---|---|---|---|---|---|---|---|---|
| | | | 100 | 11.300 | | | | |
| | | | 110 | 7.990 | | 100 | | |
| 111 | | 111 | 111 | 6.524 | | | | |
| 200 | | | 200 | 5.650 | (100) | 100,002 | 001 | 001 |
| | | | 210 | 5.054 | | 101 | | |
| | | | 211 | 4.613 | | | | |
| 220 | | 220 | 220 | 3.995 | (110) | 110,102 | 200 | |
| | | | 300 | 3.767 | | 003 | | |
| | | | 310 | 3.573 | | | | |
| | | | 311 | 3.407 | | | 311 | |
| [222] | [222] | [222] | 222 | 3.262 | 111 | 112 | 222 | 002 |
| | | | 320 | 3.134 | | 103 | | |
| | | | 321 | 3.020 | | | | |
| [400] | [400] | [400] | 400 | 2.825 | 200 | 200,004 | 400 | |
| | | | 410 | 2.741 | | 201 | | |
| | | | 330,411 | 2.663 | | | | |
| | | | 331 | 2.592 | | | 331 | |
| | | | 420 | 2.527 | (210) | 210 | 420 | |
| | | | 421 | 2.466 | | 211 | | |
| | | | 332 | 2.409 | | | | |
| | | | 422 | 2.307 | (211) | 212 | 422 | |
| 500 | 500 | | 500 | 2.260 | | 203,005 | | |
| | | | 510 | 2.216 | | | | |
| | | | 333 | 2.175 | | 213 | 333 | |
| | | | 432 | 2.098 | | | | |
| | | | 521 | 2.063 | | | | |
| [440] | [440] | [440] | 440 | 1.998 | 220 | 220,204 | 440 | 110 |

*Standard cubic reflections of the GaAs type are in square brackets.
**Additional reflections for the primitive structure are in parentheses.

52

Table 8. Continued

| Q1-72 Ga-In-P-As hkl | Q1-75 InP$_{0.34}$As$_{0.66}$ hkl | Q2-012 Ga$_{0.47}$In$_{0.53}$As a=11.30 hkl | Prim. Cubic As a=11.30 hkl | d | Würtzite derivative Hex. a=2a=7.99030 c=6.52405 hkl | BeSiN$_2$ Orth. a=7.99030 b=6.98980 c=6.52405 hkl | 4H Hex. a=3.99515 c=13.036 hkl | 6H Hex. a=3.99515 c=19.57215 hkl | 8H Hex. a=3.99515 c=26.09610 hkl |
|---|---|---|---|---|---|---|---|---|---|
| | | | 100 | 11.300 | | | | | |
| | | | 110 | 7.990 | | 100 | | | |
| 111 | | 111 | 111 | 6.524 | 001 | 001 | 002 | 003 | 004 |
| 200 | | | 200 | 5.650 | | | | | |
| | | | 210 | 5.054 | | | | | |
| | | | 211 | 4.613 | | 101 | | | |
| 220 | | 220 | 220 | 3.995 | 110 | 200 | | 010 | 010 |
| | | | 300 | 3.767 | | | | | |
| | | | 310 | 3.573 | | | | | |
| | | | 311 | 3.407 | | 201 | | 013 | 014 |
| [222] | | [222] | 222 | 3.262 | 002 | 002 | 004 | 006 | 008 |
| | | | 320 | 3.134 | | | | | |
| | | | 321 | 3.020 | | 102 | | | |
| [400] | | [400] | 400 | 2.825 | | | | | |
| | | | 410 | 2.741 | | | | | |
| | | | 330,411 | 2.663 | | 300 | | 110 | 110 |
| | | | 331 | 2.592 | | | | 113 | 114 |
| | | | 420 | 2.527 | 112 | 202 | | 016 | 018 |
| | | | 421 | 2.466 | | 301 | | | |
| | | | 332 | 2.409 | | | | | |
| | | | 422 | 2.307 | 030 | 030 | | | |
| 500 | 500 | | 500 | 2.260 | | | | | |
| | | | 510 | 2.216 | | | | | |
| | | | 333 | 2.175 | 003 | 103 | 006 | 009 | 00 12 |
| | | | 432 | 2.098 | | 302 | | | |
| | | | 521 | 2.063 | | | | | |
| [440] | | [440] | 440 | 1.998 | 220 | 400,230 | 110 | 020 | 020 |

53

Table 8. Continued

| Q1-72 Ga-In-P-As hkl | Q1-75 $InP_{0.34}As_{0.66}$ hkl | Q2-012 $Ga_{0.47}In_{0.53}As$ hkl | Prim. Cubic a = 11.30 hkl | d | 9R Rhom. a = 3.99515 c=29.35822 hkl | 10H Hex. a=.3.99515 c=32.62025 hkl | 12R Rhom. a=3.99515 c=39.14430 hkl | 15R Rhom. a = 3.99515 c=48.93037 hkl |
|---|---|---|---|---|---|---|---|---|
|  |  |  | 100 | 11.300 |  |  |  |  |
|  |  |  | 110 | 7.990 |  |  |  |  |
| 111 | 111 | 111 | 111 | 6.524 |  | 005 | 006 |  |
| 200 |  |  | 200 | 5.650 |  |  |  | 010 |
|  |  |  | 210 | 5.054 |  |  |  |  |
|  |  |  | 211 | 4.613 |  |  |  |  |
| 220 | 220 | 220 | 220 | 3.995 | 010 | 010 | 010 | 010 |
|  |  |  | 300 | 3.767 |  |  |  |  |
|  |  |  | 310 | 3.573 |  |  |  |  |
|  |  |  | 311 | 3.407 |  | 015 | 016 |  |
| [222] | [222] | [222] | 222 | 3.262 | 009 | 00 10 | 00 12 | 00 15 |
|  |  |  | 320 | 3.134 |  |  |  |  |
|  |  |  | 321 | 3.020 |  |  |  |  |
| [400] | [400] | [400] | 400 | 2.825 | 110 | 110 | 110 | 110 |
|  |  |  | 410 | 2.741 |  |  |  |  |
|  |  |  | 330,411 | 2.663 |  |  |  |  |
|  |  |  | 331 | 2.592 |  |  |  |  |
|  |  |  | 420 | 2.527 |  |  |  |  |
|  |  |  | 421 | 2.466 | 019 | 115 | 116 | 01 15 |
|  |  |  | 332 | 2.409 |  | 01 10 | 01 12 |  |
|  |  |  | 422 | 2.307 |  |  |  |  |
| 500 |  |  | 500 | 2.260 |  |  |  |  |
|  |  |  | 510 | 2.216 |  | 00 15 | 00 16 |  |
|  |  |  | 333 | 2.175 |  |  |  |  |
|  |  |  | 432 | 2.098 |  |  |  |  |
|  |  |  | 521 | 2.063 |  |  |  |  |
| [440] | [440] | [440] | 440 | 1.998 | 020 | 020 | 020 | 020 |

## III. DISCUSSION AND RECOMMENDATION FOR FUTURE RESEARCH

The present approach is purely geometrical and is based on crystal symmetry arguments. No detailed energetic consideration is given, since it is as difficult to theoretically determine which structure is most stable in any particular case, as it is to decide whether a given metal will crystallize in a FCC, BCC, or HCP crystal. In both cases, the criterion is the maximization of the cohesive energy.

After all these surveys, the superstructure reflections found in two ternary and one quaternary compositions, are not explained by any simple atomic arrangement. Structures that readily suggest them-selves, namely, the ZnS polytypes 2H, 4H, 6H, 8H, 9R, 10H, 12R, 15R, 21R, the tetragonal chalcopyrite structure, the orthorhombic $BeSiN_2$ structure, ordering of the anion or cation sublattice, as in Cu-Au or Cu-Pt , all do not account for the observed and missing extra reflec-tions.

The experimental observation of additional reflections in the crystals of compositions $Ga_{0.19}In_{0.81}P_{0.10}As_{0.90}$ , $Ga_{0.01}In_{0.99}P_{0.34}As_{0.66}$, and $Ga_{0.47}In_{0.53}As$ suggest that some derivative superstructure of the GaAs type is being formed. The reported tendency toward clustering in $Ga_{0.5}In_{0.5}P$ [30] seems to contradict this conclusion, because ordering and clustering represent opposite thermodynamic tendencies that are not usually compatible. It should be pointed out that the present study does not include the above phosphide and that the gallium-indium-arsenide

need not behave as the phosphide. On the other hand, it is also possible that the alloys studied in the present investigation segregate into two phases, both of which have "tetrahedral" structures. The structure of the new phase will then have to be characterized as a derivative of GaAs with details as yet undetermined.

For further structure analysis, the following is recommended:

1. Increasing the intensity of superstructure reflections is essential. This may be attained by:

(1) Annealing of the crystal to eliminate the thermal disorder factor.

(2) Using Cukα radiation.

Shorter wavelength (Mokα radiation) was used for initial study to increase the number of accessible points in reciprocal lattice. Cukα radiation may be applied for further study for its imposed effect of modifying atomic scattering factors. This is estimated as the following:

| | Atomic No. | $\lambda k$ (k Absorb. Edge) | Mokα $\lambda/\lambda k$ | Cukα $\lambda/\lambda k$ | $\Delta f$ |
|---|---|---|---|---|---|
| In | 49 | 0.444 | 1.599 | 3.474 | - |
| Ga | 31 | 1.195 | 0.594 | 1.290 | -2.2 |
| P | 15 | 5.787 | 0.123 | 0.266 | - |
| As | 33 | 1.045 | 0.679 | 1.476 | -1.8 |

$\lambda/\lambda k < 0.8$, $\Delta f$ correction is negligible;

$\lambda/\lambda k > 1.6$, $\Delta f$ correction is about constant and independent of variation in $\lambda k$ .

The contribution of Ga and As scattering to those reflections that are strongly dependent on the difference $f_{Ga} - f_{As}$ can be enhanced by using $CuK\alpha$ radiation instead of $MoK\alpha$ radiation.

$$I \propto (f_{Ga} - f_{As})^2 \cong (31 - 33)^2 = 4$$

$$I \propto (f'_{Ga} - f'_{As})^2 \cong [(31 - 2.2) - (33 - 1.8)]^2 = 5.76 .$$

2.  Rhombohedral derivative structure model should be applied. It is likely the case, since differential thermal expansion along [111] and inclined dislocations [31,32] resulting from LPE growth would account for the rhombohedral structure, according to Verma and Krishna [32]. Space group R3m (lowest rhombohedral symmetry that can be exhibited by a periodic stacking of close packed layers) [32] may describe the 64-atom unit cell, 961 hypothetical compositions, and more than one thousand arrangements may be generated.

Perhaps the best and quickest clue is to use TEM lattice imaging for primary deduction and following the refining by x-ray diffraction.

APPENDIX B


Proposed Quaternary Alloy Semiconductor MESFET (QFET) Designs

for Operation in X and Ka Bands

R. J. Trew

# I. INTRODUCTION

This report presents proposed device designs for MESFETs capable of low-noise, small-signal amplification of RF signals in the X (8-12 GHz) and Ka (26-40 GHz) band frequency ranges. The devices are fabricated from quaternary alloy $Ga_{0.27}In_{0.73}P_{0.4}As_{0.6}$ epitaxial layers grown on semi-insulating InP substrates. Standard one-micron gate length technology is to be utilized for the fabrication of the X-band device. Operation in Ka band represents a significant advance in the current state of the art, and improved technology will be required in order to fabricate the required submicron-sized gate length devices. The Ka band structure is designed with a 0.2 μm gate length. Standard 0.5-μm gate length technology could be used to fabricate the Ka band MESFET as demonstrated by the results of Krumm et al. [33]. Using a 0.5-μm GaAs MESFET, they constructed and operated an amplifier for Ka band operation and obtained 11 db gain at 33 GHz with a 5.5-db noise figure. A shorter gate length should lead to improved performance.

The design procedure and calculations are presented. Design compromises were made on the basis of technological, material, and device operation criteria; and the rationale for the various decisions are presented. Much of the design is based on the small-signal model of Pucel, Haus, and Statz [34]. This model has been used by various workers to accurately predict device performance. In order to get a feeling for the performance that can be anticipated from these devices, certain figures of merit are calculated.

## II.  DESIGN PROCEDURE

The X band MESFET is shown in Figures 15-17 and is designed with a
one-micron long gate.  The material and design parameters are listed in
Tables 9 and 10.  One-micron gate GaAs MESFETs are extensively used in the
microwave industry for a wide variety of applications and provide excel-
lent performance.  With the same technology and the improved parameters of
the quaternary alloy semiconductor material, improved device characteris-
tics should be obtained.  The frequency response and noise figure of the
device are critically dependent upon the gate length.  Although the one-
micron gate is near optimum for X band operation, shorter gates are required
for Ka band.  There is a limit to performance improvements from gate length
reduction although the gate length limit is not precisely known.  Commer-
cial GaAs MESFETs are available with 0.5 μm gate lengths, and experimental
devices have been produced with 0.25 μm gates.  The Ka band device is
designed with a 0.2 μm gate, and state-of-the-art fabrication techniques
will be required.  There is not much information available on the operation
of such short gate length devices, and the RF performance may be signifi-
cantly affected by velocity overshoot considerations.  This subject requires
further research the Ka band MESFET is shown in Figures 18-20, and its
design parameters are listed in Table 10.

The width, Z, of the gate affects the RF output power, the device gain,
and almost all of the equivalent circuit elements.  It has a significant
effect upon the gate resistance, Rg.  Although the gate is a transmission
line, it can be modeled with lumped elements as long as the gate width is
short compared to the RF wavelength.  In order to avoid distributed effects,
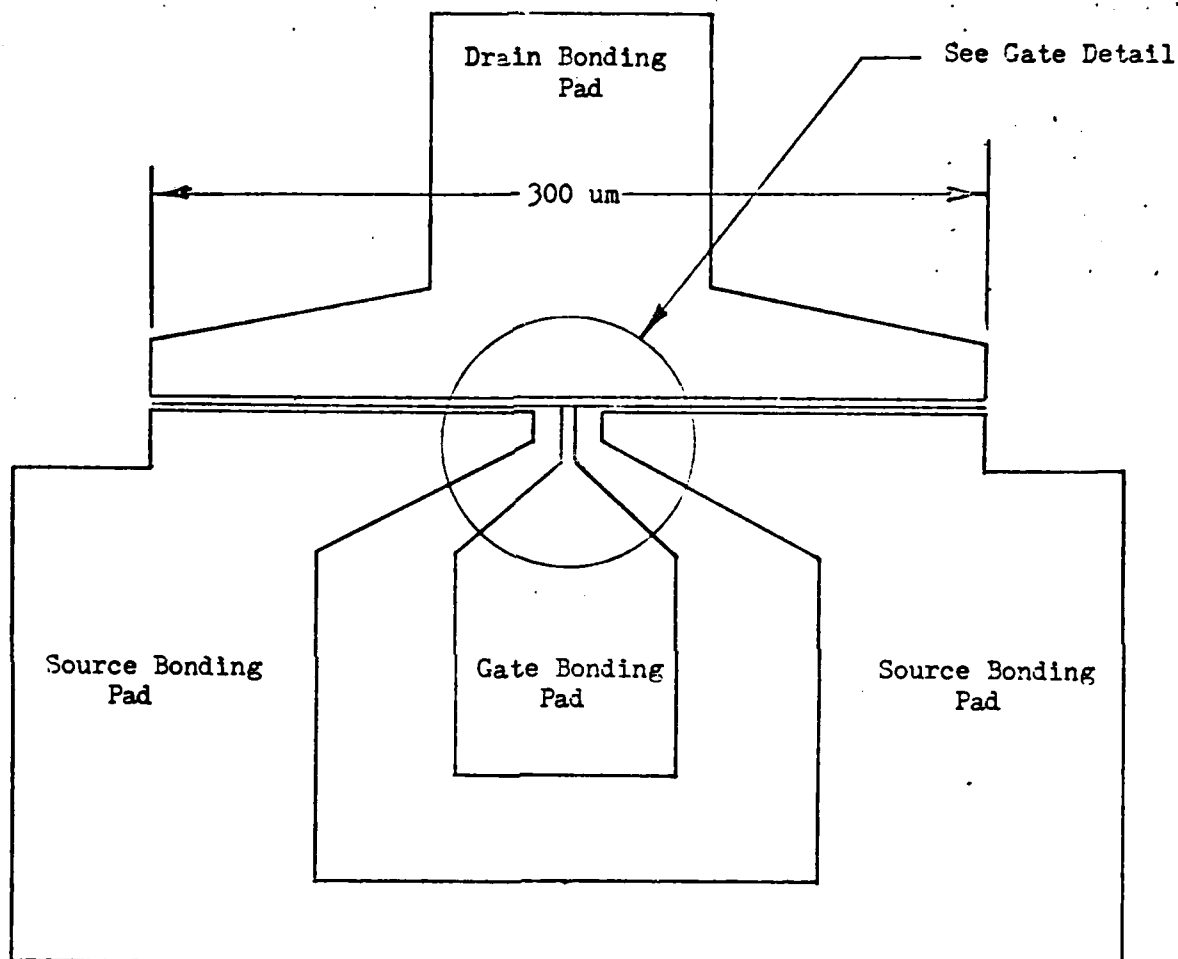the gate length should be no more than approximately 0.04 λ in the long

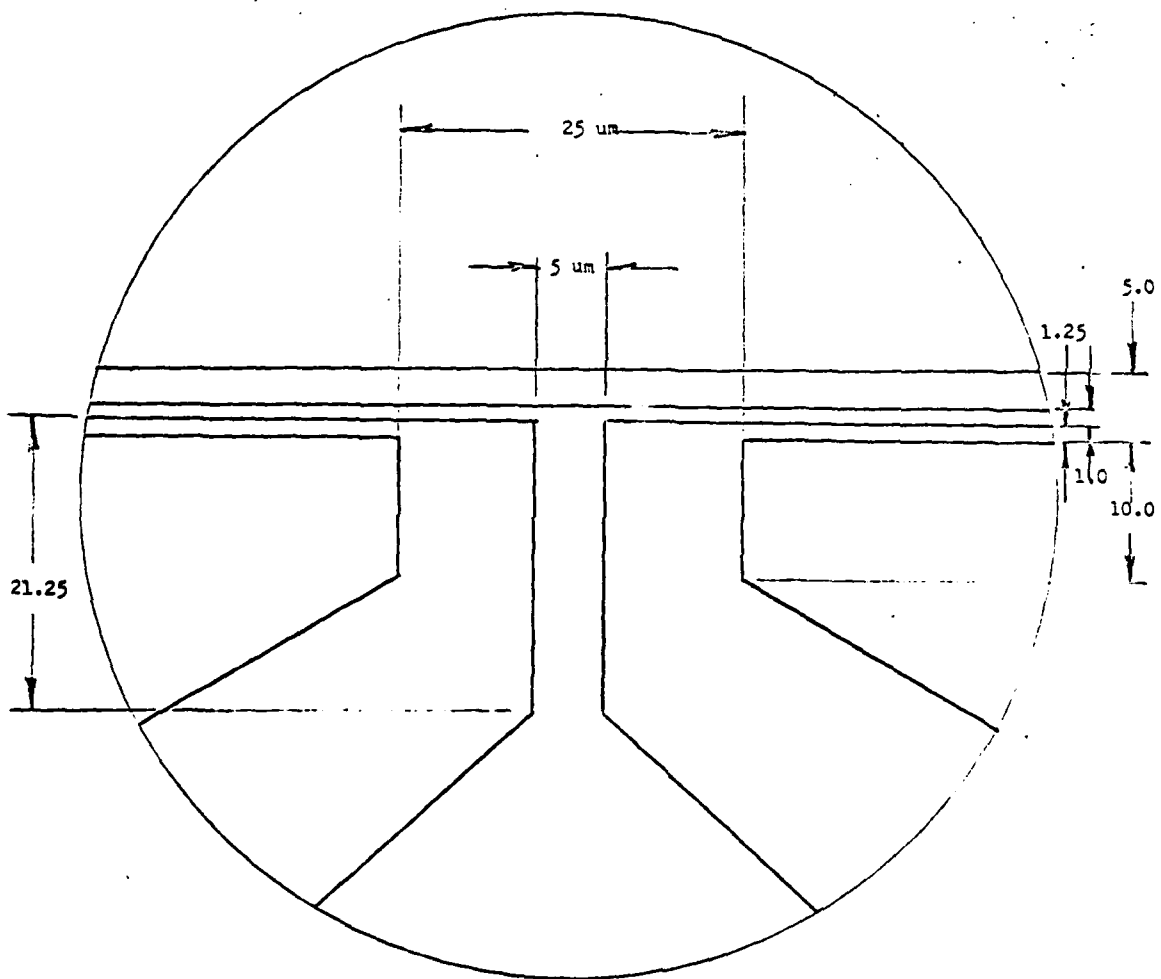Figure 15.   X-Band Low-Noise MESFET Layout
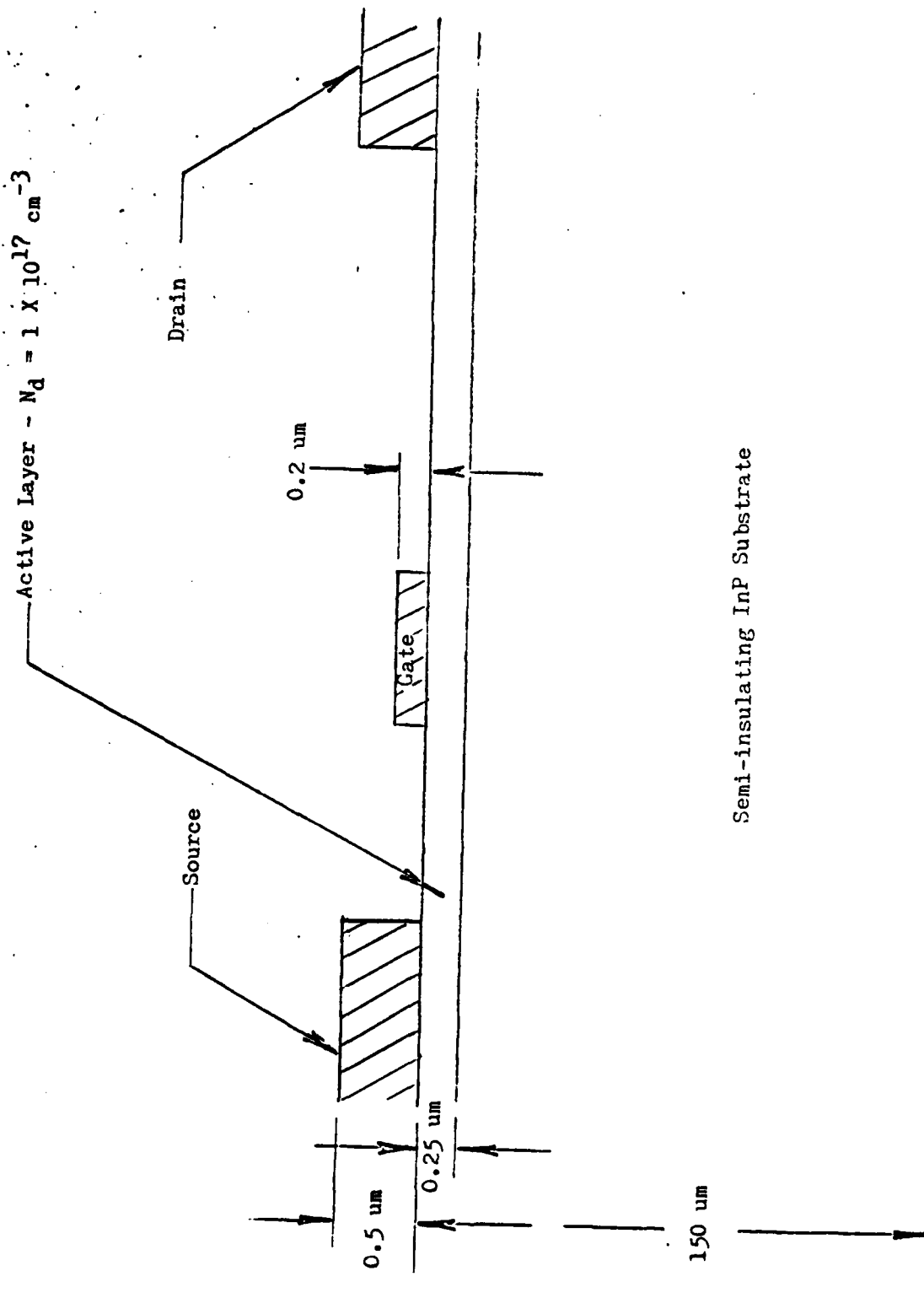
Figure 16.    X-Band MESFET Gate Detail

Figure 17. X-Band MESFET--Cross Section

64

Table 9. Material Parameters for $Ga_{0.27}In_{0.73}P_{0.4}As_{0.6}$ Used in MESFET Design

$$\varepsilon_R = 13.2$$

$$\varepsilon_o = 8.854(10)^{-14} \text{ F/cm}$$

$$E_s = 5(10)^3 \text{ V/cm}$$

$$v_p = 2.8(10)^7 \text{ cm/sec}$$

$$v \ (@ \ 8 \text{ kV/cm}) = 2(10)^7 \text{ cm/sec}$$

$$\rho_s(\text{x-band}) = 350 \ \Omega/\square$$

$$\rho_s(\text{Ka-band}) = 366 \ \Omega/\square$$

Table 10. Design Parameters

|  | X-Band Device | Ka-Band Device |
|---|---|---|
| $N_d$ (cm$^{-3}$) | $1 \times 10^{17}$ | $2.4 \times 10^{17}$ |
| $L_g$ (cm) | $1 \times 10^{-4}$ | $0.2 \times 10^{-4}$ |
| $L_{sd}$ (cm) | $5 \times 10^{-4}$ | $2.5 \times 10^{-4}$ |
| $L_{gd}$ (cm) | $2.75 \times 10^{-4}$ | $1.15 \times 10^{-4}$ |
| a (cm) | $0.25 \times 10^{-4}$ | $0.1 \times 10^{-4}$ |
| (cm) | $150 \times 10^{-4}$ | $100 \times 10^{-4}$ |
| (cm) | $300 \times 10^{-4}$ | $100 \times 10^{-4}$ |
| N | 2 | 2 |

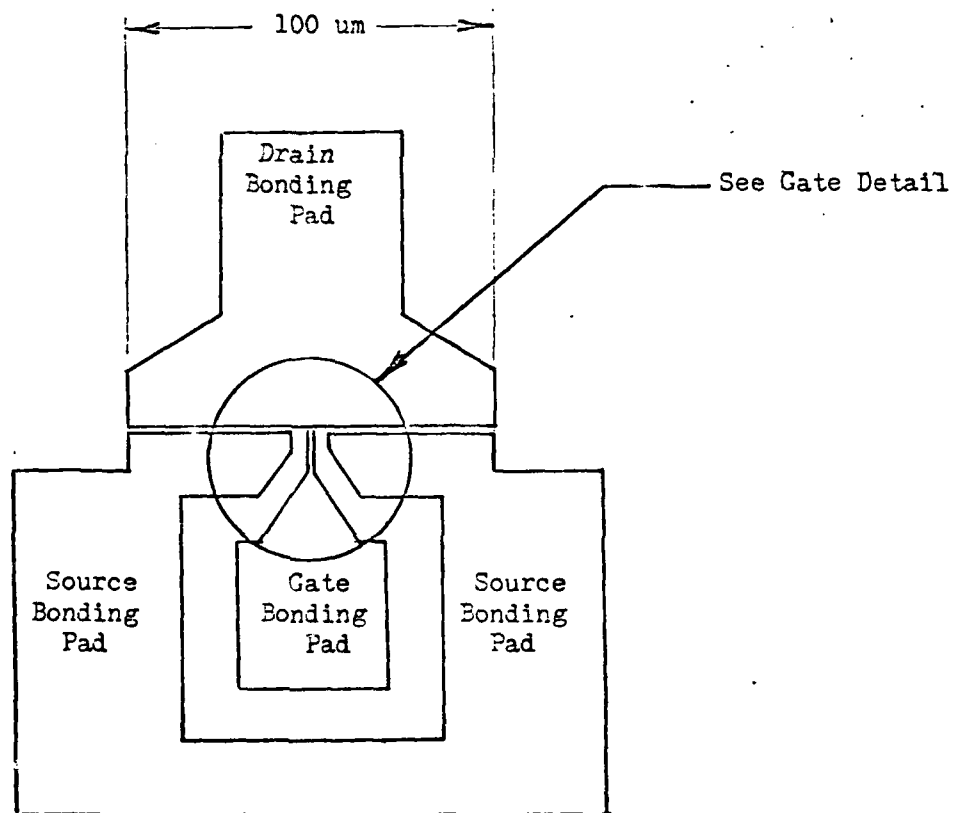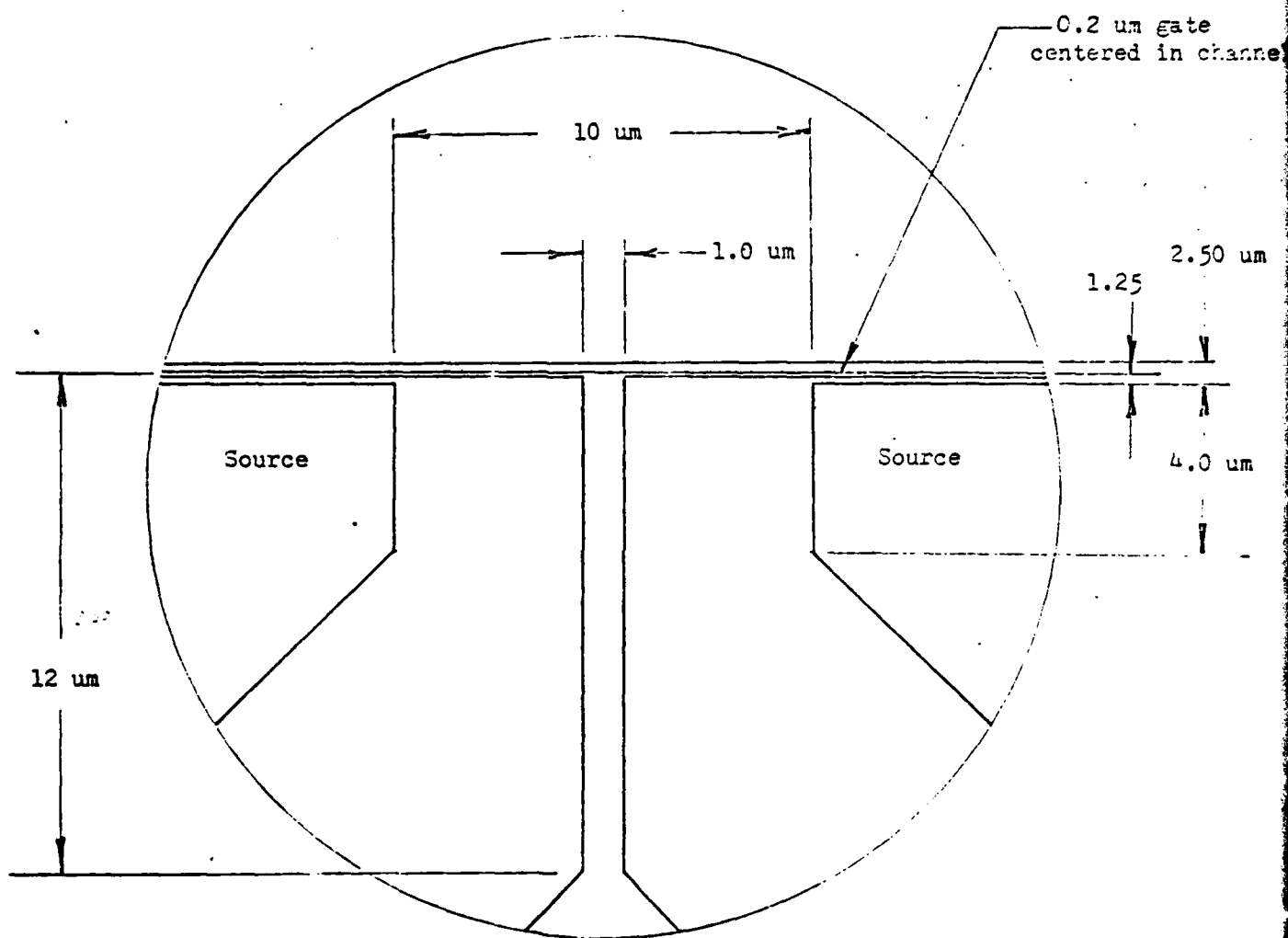Figure 18.  Ka-Band MESFET--Device Layout.
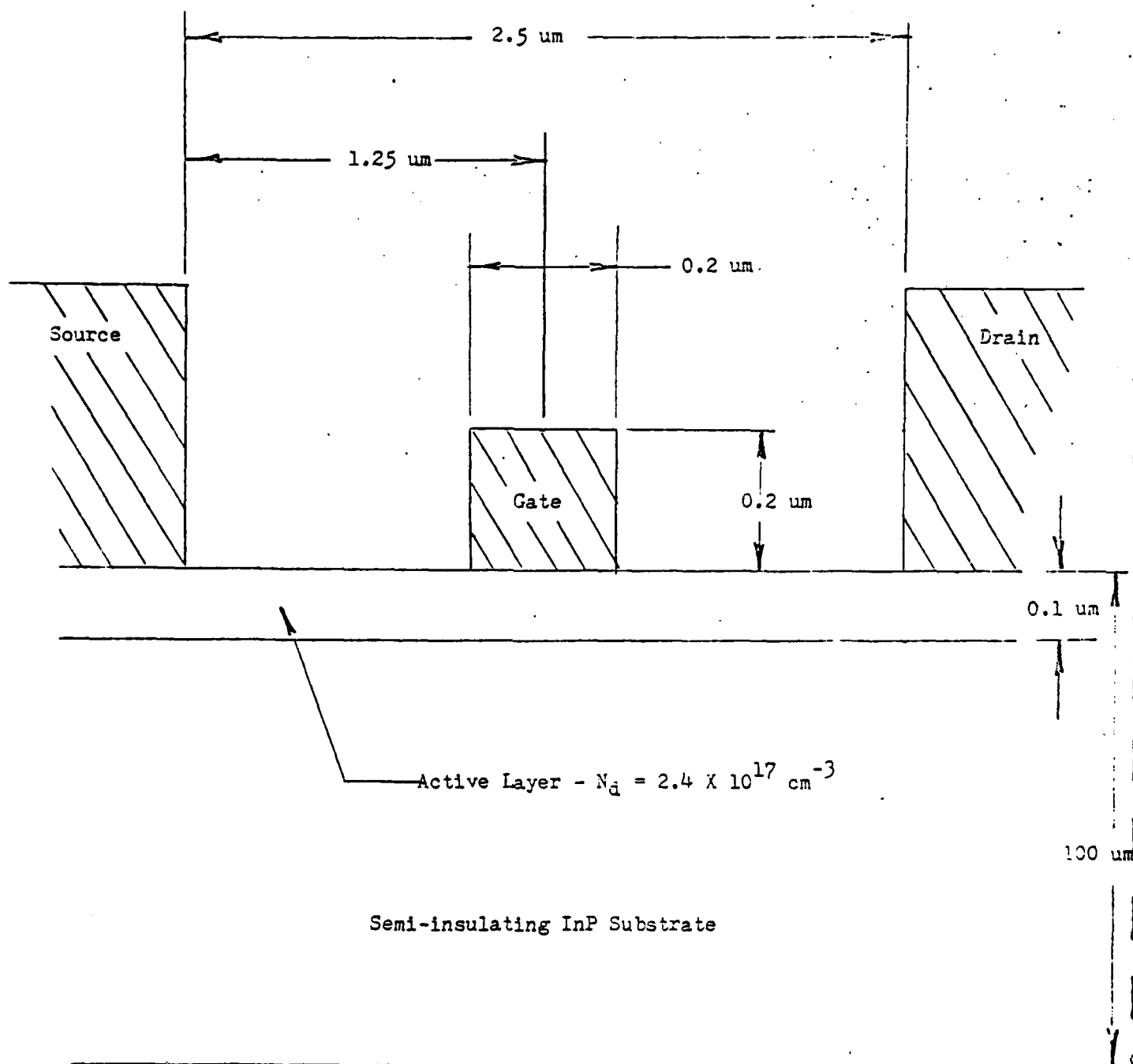
Figure 19.   Ka-Band MESFET--Gate Detail.

Figure 20.  Ka-Band MESFET—Cross Section.

dimension. The X band device is designed with a 300-μm gate width, and the Ka band device has a 100-μm gate width. The gates of these devices, therefore, can be modeled as lumped elements. The gate spacing in the channel has a significant effect upon the operation of the device since the device capacitances are a strong function of geometry. Generally it is desirable to minimize the gate-to-drain feedback capacitance, and the gate is located asymmetrically in the channel with the gate-to-drain spacing larger than the gate-to-source distance. Also, the gate channel width significantly affects the power handling capability of the device since the dc voltage that can be applied is dependent upon this parameter. The limit to the dc voltage is determined by the drain-to-source breakdown voltage, which for GaAs devices can be expressed approximately as

$$V_{Bds} \approx 3.5 \; (L_{sd})^{2/3} \; .$$

For high power devices, therefore, it is desirable to have large source-to-drain spacings. This, of course, conflicts with high frequency response, since the device is transit-time limited at high frequencies. The X band device as a 5-μm spacing with the gate located 2.75 μm from the drain. The Ka band device has a 2.5-μm gate channel with the gate centered in the channel. The centered channel design for the Ka band device was selected to simplify the fabrication. Selection of a gate metal must be an experimental procedure. There is very little information available on Schottky contacts on the quaternary alloys, and more research in this area is required.

The epitaxial layer thickness and impurity doping density are selected based on experience with GaAs MESFETs. The best devices have $(N_d)$ X thickness (a) products of about $2.4 \times 10^{12}$ cm$^{-2}$. Highly doped active layers are

69

preferred because of the ease of forming drain and source ohmic contacts and because of the reduction in the semiconductor resistivity. A reduction in resistivity produces lower noise figures. A limit to the doping concentration is dependent on technological considerations and the reduction in the gate-to-channel breakdown voltage. Practical doping concentrations are in the range of $5 \times 10^{16}$ to $4 \times 10^{17}$ $cm^{-3}$ in GaAs MESFET epitaxial layers. The X band device is designed with $N_d = 1 \times 10^{17}$ $cm^{-3}$ and a = 0.25 µm; the Ka band device with $N_d = 2.4 \times 10^{17}$ $cm^{-3}$ and a = 0.1 µm.

The center-fed gate geometry (Figures 15 and 18) was selected in order to maximize the RF power handling capability and the gain while maintaining a low input impedance. The source pad area was maximized to provide a low inductive path to RF ground. Any source inductance will provide feedback that will increase the device noise figure and decrease stability.

The bonding pads for the source, drain, and gate are large enough to accommodate 0.7-mil gold bonding wires located far enough away from the gate area so that the active region will not be damaged by thermocompression bonding. The source and drain ohmic contacts are to be formed from a AuGe/Ni/Au metal system. The bonding pads will be formed by a gold film overlay.

The overall thickenss of the MESFET chips are selected to be 150 µm and 100 µm for the X and Ka band devices, respectively. Mechanical handling and parasitic capacitance considerations are factors in the selection of these particular values. Semi-insulating InP is used as the substrate material, and the bulk resistivity should have a minimum value of about $10^8$ $\Omega \cdot cm$.

# III.  EQUIVALENT CIRCUIT AND ELEMENT VALUE CALCULATIONS

An equivalent circuit that can be used to predict the small-signal operation of the MESFET devices is shown in Figure 21.  This circuit is based on the model of Pucel, Haus, and Statz.  The circuit element values are listed in Table 11 and were calculated in the following manner.

1.  The gate resistance, $R_g$, is due to the geometry and resistivity of the gate metallization.  It has been shown [35] that the gate RF resistance of short gate devices is one-third the dc resistance.  Therefore,

$$R_g = \frac{\rho_g Z}{3N t_g L_g}$$

where $\rho$ = the resistivity of the gate metallization (for Au, $\rho_g \simeq$ $3(10)^{-6}$ $\Omega \cdot cm$)

$Z$ = gate width

$t_g$ = gate thickenss

$L_g$ = gate length

$N$ = number of gate fingers ($N = 2$).

2.  The source and drain resistances, $R_s$ and $R_d$, are the sums of all the resistance contributions from the bonding pads to the edges of the gate depletion region.  These resistances include contributions from the contact resistance between the metal and the epitaxial layer and the sheet resistance of the semiconductor material between the edge of the ohmic contacts and the gate.  The resistance values can be calculated from the equations

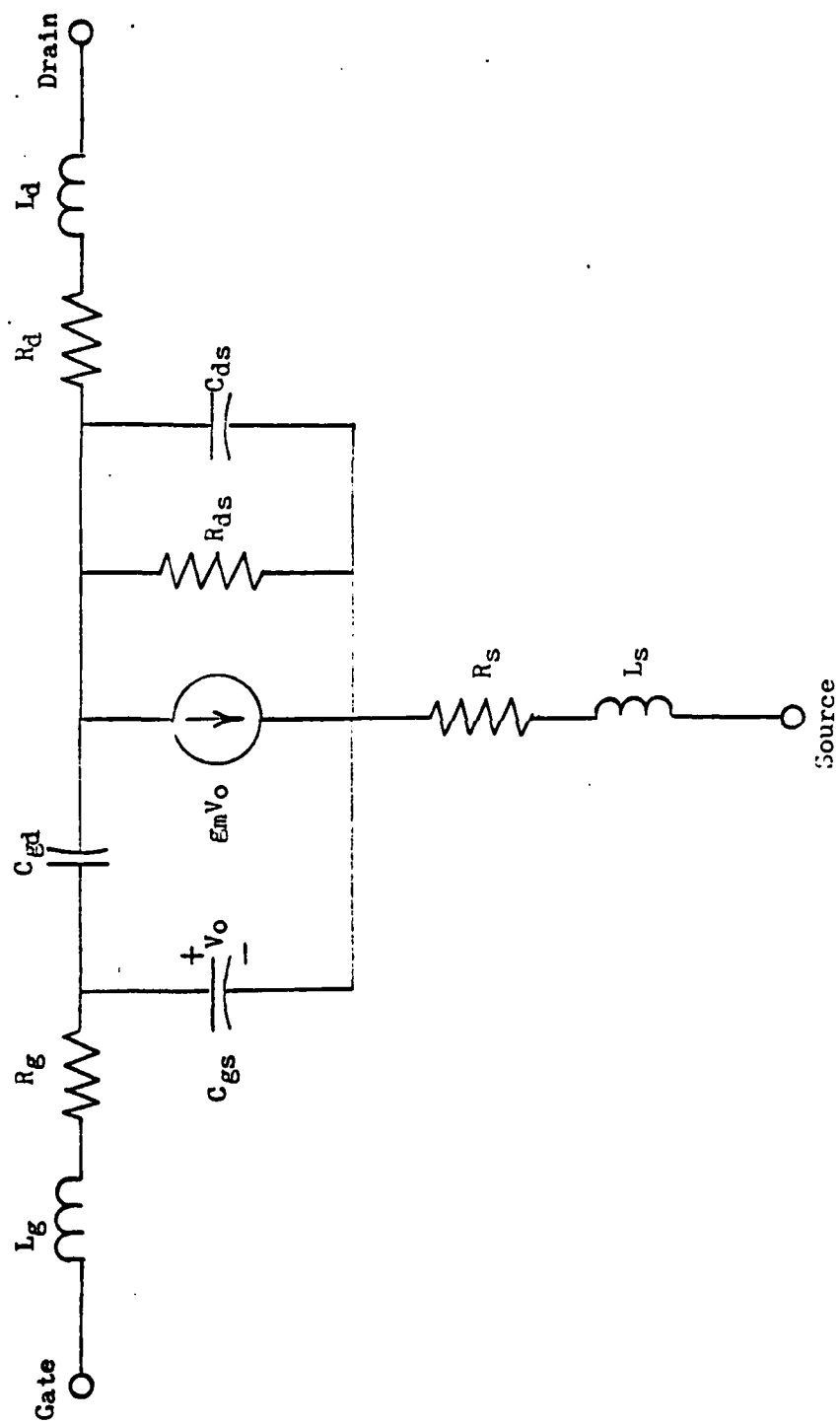$$R_s = \rho_s \frac{L_{gs}}{Z} + \frac{R_c}{Z}$$

Figure 21.  MESFET Small-Signal Equivalent Circuit.

72

Table 11. Equivalent Circuit Element Values

|  | X Band Device | Ka Band Device |
| --- | --- | --- |
| $R_g$ ($\Omega$) | 7.5 | 12.5 |
| $R_d$ ($\Omega$) | 4.80 | 9.21 |
| $R_s$ ($\Omega$) | 3.13 | 9.21 |
| $C_{gs}$ (pF) | 0.439 | 0.0915 |
| $C_{gd}$ (pF) | 0.036 | 0.0086 |
| $C_{ds}$ (pF) | 0.061 | 0.021 |
| $R_{ds}$ ($\Omega$) | 762 | 1142 |
| gm (mmho) | 66 | 55 |

and

$$R_d = \rho_s \frac{L_{dg}}{Z} + \frac{R_c}{Z}$$

where $\rho_s$ is the semiconductor sheet resistivity (listed in Table 9), $L_{gs}$ and $L_{dg}$ are the spacings between the gate and the source and drain electrodes, and $R_c$ is the contact resistance.

The contact resistance, $R_c$, is not known for the quaternary layers and is estimated to be approximately 0.05 $\Omega \cdot$cm. Threr could be considerable error in this number, and the exact value needs to be experimentally established.

3. The output resistance, $R_{ds}$, is the resistance between the drain and source with the channel operating in velocity saturation. It can be calculated from the expression

$$R_{ds} = \frac{\pi |V_{ds}|}{4E_s \epsilon_R \epsilon_o v_s Z} \left(1 - \frac{I_d}{I_s}\right)$$

where $V_{ds}$ = drain-to-source voltage

$E_s$ = saturation field

$\epsilon_R$ = semiconductor relative permittivity

$v_R$ = carrier velocity at the bias field

$I_d$ = drain bias current

$I_s$ = drain current with no gate bias.

It has been shown [36] that for optimum low-noise operation the device should be biased so that

$$\frac{I_d}{I_s} = 0.15 \ .$$

The drain-to-source voltage is selected so that the bias field in the channel is

$$E_s = 8 \text{ kV/cm} \ ,$$

and this results in a carrier velocity of

$$v_s = 2 \times 10^7 \text{ cm/sec} \ .$$

4. The drain-to-source capacitance, $C_{ds}$, is primarily a function of the geometry between the source and drain electrodes. It can be calculated from the expression

$$C_{ds} = \frac{(\epsilon_R + 1)\epsilon_o ZK[(1 - k_{ds}^2)^{1/2}]}{K(k_{ds})}$$

where

$$k_{ds} = \left[\frac{(L_s + L_d + L_{sd})L_{sd}}{(L_s + L_{sd})(L_d + L_{sd})}\right]^{1/2}$$

and $L_s$, $L_d$ are the effective source and drain electrode lengths and $L_{sd}$ is the source-to-drain spacing. The functions K are complete elliptic integrals of the first kind.

5. The feedback capacitance, $C_{gd}$, can be calculated in the same manner. That is,

$$C_{gd} = \frac{(\epsilon_R + 1)\epsilon_o ZK[(1 - k_{gd}^2)^{1/2}]}{K(k_{gd})}$$

where

$$k_{gd} = \left[\frac{L_{dg}}{L_{dg} + L_g}\right]^{1/2}$$

and $L_{dg}$ is the drain-to-gate spacing.

6. The gate-to-source capacitance, $C_{gs}$, is particularly important since it significantly affects the device frequency response. It can be calculated from the expression

$$C_{gs} = \epsilon_R \epsilon_o Z\left[\frac{L_g}{a}\left(\frac{1}{1 - I_d/I_s}\right) + 1.56\right]$$

where a is the active layer thickness. This expression shows the advantage of a short gate length and of a low $I_d/I_s$ ratio for minimizing $C_{gs}$. The last term in the expression describes the parasitic capacitance that results from the curvature of the depletion region at the edge of the gate.

7. The gain of the defice is dependent upon the MESFET transconductance, $g_m$. This parameter can be calculated with the equation

$$g_m = \frac{2\epsilon_R \epsilon_o v_s Z}{a} \left[ \frac{1}{1 - I_d/I_s} \right].$$

As can be seen, a high $v_s$, large Z, and small a are desirable to produce a large transconductance. The bias conditions also have a significant effect upon this parameter, and for optimum gain, $I_d/I_s$ should be maximized. Such a bias condition, however, results in an increase in the device noise figure, and the requirements for maximum gain and low-noise operation are in conflict.

8. The inductances $L_x$, $L_g$, and $L_d$ represent the bond wires that must be used to interface the device with the RF circuit. If 0.7-mil gold wire is used, the inductances can be calculated from the relationship

$$50 \text{ mil} \approx 1 \text{ nh} .$$

Parallel wires would, of course, reduce the parasitic inductance.

## IV. FIGURES-OF-MERIT AND BIAS CONDITIONS

The anticipated performance of these devices are indicated by calculation of certain figures-of-merit. The calculated numbers are listed in Table 12 and were determined in the following manner.

(a) Cutoff frequency is the frequency at which the forward current gain is unity. It can be thought of as the gain-bandwidth product and can be expressed as

$$f_T \simeq \frac{g_m}{2\pi C_{gs}} \quad .$$

(b) The maximum frequency of oscillation is the frequency at which the device matched power gain has decreased to unity and is expressed as

$$f_{max} \simeq \frac{f_T}{2\sqrt{r+f_T\tau}}$$

where

$$r = \frac{R_g + R_s}{R_{ds}}$$

and

$$\tau = 2\pi R_g C_{dg} \quad .$$

(c) Mason's unilateral gain is approximately

$$U \simeq \left(\frac{f_{max}}{f}\right)^2 \quad .$$

It is, of course, desirable to maximize all of these figures-of-merit for optimum RF performance.

The MESFET bias conditions were also calculated and are listed in Table 13. The calculated values were determined in the following manner.

(d) The drain current with zero gate bias, $I_s$, is given by the expression

$$I_s = a \, q\mu N_d Z E_s$$

where $\mu m$ is the low-field mobility.

(e) The dc bias current was determined from the low-noise bias condition that

$$I_d = 0.15 \, I_s \, .$$

(f) The drain-to-source bias voltage and the gate voltage are to be adjusted to provide the correct bias current. An estimate for $V_{ds}$ is obtained by requiring the channel field to be sufficient for velocity saturation. The channel field was selected to be 8 kV/cm.

(g) The gate pinch-off voltage can be determined from the expression

$$V_{pinch-off} \approx \frac{qN_d a^2}{2\epsilon_R \epsilon_o} \, .$$

Table 12.  Calculated Figures-of-Merit

|  | X-Band Device | $K_a$-Band Device |
|---|---|---|
| Cutoff Frequency, $f_T$ | 23.9 GHz | 95.7 GHz |
| Max. frequency of Oscillation, $f_{max}$ | 51.2 GHz | 165 GHz |
| Unilateral Gain, U | 12.6 db @ 12 GH | 12.3 db @ 40 GHz |

Table 13.  Device dc Parameters

|  | X-Band Device | $K_a$-Band Device |
|---|---|---|
| $I_{dss}$ (mA) | 427 | 136 |
| $I_{ds}$ (mA) | 64 | 20.5 |
| $V_{ds}$ (v) | 4 | 2 |
| $V_{pinch-off}$ (v) | 4.28 | 1.64 |

# V. SUMMARY

Designs for MESFETs capable of X- and Ka-band operation have been presented. The X-band device utilizes standard one-micron gate length technology. An optimized Ka-band MESFET, however, will require state-of-the-art fabrication technology. The devices are intended to take advantage of the favorable material parameters of the quaternary alloy $Ga_{0.27}In_{0.73}P_{0.4}As_{0.6}$ material system lattice matched to semi-insulating InP substrates. Such devices should provide improved performance over comparable GaAs devices.

An equivalent circuit based upon the model of Pucel, Haus and Statz has been derived for the devices. The equivalent circuit can be used for predictions of device performance. Much of the MESFET design was based upon the optimization of the model circuit elements.

An indication of device performance is given by the calculated figures-of-merit. These calculations indicate that the MESFET devices have considerable potential as low-noise, high-gain microwave and millimeter wave amplifiers.

REFERENCES

1. J. W. Harrison, J. R. Hauser, T. H. Glisson, and M. A. Littlejohn, "Advanced III-V Compound Materials Study," AFAL-TR-77-129, Final Report on Contract F33615-76-C-1265 (WPAFB/AFAL/DHM-1), Research Triangle Institute, Research Triangle Park, NC, July 1977.

2. G. A. Antypas and R. L. Moon, J. Electrochem. Soc. 120, 1574 (1973).

3. R. Sankaran, et al., J. Vac. Sci. and Technol. 13, 932 (1976).

4. J. J. Hsieh, M. C. Finn, and J. A. Rossi, J. Electronic Mater. 1, 31 (1978).

5. J. J. Coleman, et al., J. Appl. Phys. 47, 2015 (1976).

6. M. A. Littlejohn, J. R. Hauser, and T. H. Glisson, Applied Phys. Letters 30, 242 (1977).

7. J. W. Harrison, et al., "Quaternary Alloy Microwave MESFET," Annual Report on AFOSR Contract No. F49620-77-C-0062, Research Triangle Institute, Research Triangle Park, NC, April 28, 1978.

8. F. E. Rosztoizy, G. A. Antypas, and C. J. Casau, International Conference on GaAs (Inst. Phys.), pp. 86-91 (1970).

9. K. E. Brown, Solid State Electron. 17, 505 (1974).

10. R. L. Moon, G. A. Antypas, and L. W. James, J. Electron. Mater. 3, 635 (1974).

11. T. H. Glisson, J. R. Hauser, M. A. Littlejohn, and C. K. Williams, J. Electron. Mater. 7, 1 (1978).

12. R. E. Nahory, M. A. Pollack, and W. D. Johnston, Jr., Appl. Phys. Lett. 33, 659 (1978).

13. K. Nakajima, A. Yamaguchi, K. Akita, and T. Kotani, J. Appl. Phys. 49, 5944 (1978).

14. P. D. Greene, S. A. Wheeler, A. R. Adams, A. N. El-Sabbahy, and C. N. Ahmad, Appl. Phys. Lett. 35, 78 (1979).

15. B. Houston, J. B. Restorff, R. S. Allgaier, and J. R. Burke, Solid State Electron. 21, 91 (1978).

16. M. A. Littlejohn, R. A. Sadler, T. H. Glisson, and J. R. Hauser, Proc. Int. Conf. on GaAs and Related Compounds, The Institute of Physics, pp. 239-247, London, 1979.

17. M. A. Littlejohn, J. R. Hauser, T. H. Glisson, D. K. Ferry, and J. W. Harrison, Solid State Electron. 21, 107 (1978).

18. B. R. Gossick, J. Appl. Phys. 30, 1214 (1959).

19. L. R. Weisberg, J. Appl. Phys. 33, 1817 (1962).

20. B. Houston, private communication.

21. N. F. Mott and W. D. Twose, Adv. Phys. 10, 107 (1960).

22. D. L. Dexter and F. Seitz, Phys. Rev. 86, 964 (1952).

23. J. W. Harrison and J. R. Hauser, J. Appl. Phys. 47, 292 (1976).

24. V. I. Fistul, Heavily Doped Semiconductors, Plenum Press, New York, NY, 1969, pp. 92-94.

25. H. Stadelmaier, et al., to be submitted for publication.

26. P. Blood and J. W. Orton, J. Phys. C: Solid State Phys. 7, 893 (1974).

27. R. G. Hamerly and M. W. Heller, J. Appl. Phys. 42, 5585 (1971).

28. H. Kressel, J. Electronic Mater. 4, 1081 (1975).

29. E. Parthé, Crystal Chemistry of Tetrahedral Structure, Gordon and Breach Science Publishers, New York, NY, 1964.

30. H. G. Brühl, et al., Phys. Stat. Sol. (a) 39, 133 (1977).

31. V. G. Bhide and A. R. Verma, Z. Krist. 111, 142 (1959).

32. A. R. Verma and P. Krishna, Polymorphism and Polytypism in Crystals, John Wiley and Sons, New York, NY, 1966.

33. C. F. Krumm, H. T. Suyematsu, and B. L. Walsh, IEEE International Microwave Symposium Digest, pp. 383-385, 1978.

34. R. A. Pucel, H. A. Haus, and H. Statz, Advances in Electronics and Electron Physics 38, 195-265 (1975).

35. P. Wolf, IBM J. Res. Develop. 14, 125-141 (March 1970).

36. C. A. Liechti, IEEE Trans. Microwave Theory Tech. MTT-24, 279-300 (June 1976).